Research Square

Preprints are preliminary reports that have not undergone peer review.
They should not be considered conclusive, used to inform clinical practice,
or referenced by the media as validated information.

NOP56 deficiency enhances poly-GP toxicity through multisystemic neurodegenerative and metabolic alterations

Ana Quelle-Regaldie
Institut des Maladies Génétiques Imagine
Manon Boivin
Institut de Génétique et de Biologie Moléculaire et Cellulaire, INSERM U 1258, CNRS UMR 7104, University of Strasbourg
Aixin Li
Institut des Maladies Génétiques Imagine
Mónica Folgueira
Universidade da Coruña
Ivan Nemazanyy
Structure fédérative de recherche Necker
Nicolas Charlet-Berguerand
Institut de Génétique et de Biologie Moléculaire et Cellulaire, INSERM U 1258, CNRS UMR 7104, University of Strasbourg
Edor Kabashi
edor.kabashi@institutimagine.org

Institut des Maladies Génétiques Imagine

Research Article

Keywords: SCA36, poly-GP, NOP56, dipeptide repeat proteins, repeat expansion disorders, neurodegeneration zebrafish.

Posted Date: November 12th, 2026

DOI: https://doi.org/10.21203/rs.3.rs-11528471/v1

License: This work is licensed under a Creative Commons Attribution 4.0 International License.
Read Full License

Additional Declarations: No competing interests reported.

NOP56 deficiency enhances poly-GP toxicity through multisystemic neurodegenerative and metabolic alterations

Ana Quelle-Regaldie[1,2], Manon Boivin[3], Aixin Li[1], Mónica Folgueira[2], Ivan Nemazanyy[4], Nicolas Charlet-Berguerand[3], Edor Kabashi[1]

1 Translational Research for Neurological Disorders, Institut Imagine, INSERM UMR 1163, Université Paris Cité, Paris, France.

2 Neurover Research Group, Centro Interdisciplinar de Química y Biología- CICA, Department of Biology, Universidade da Coruña, 15008, A Coruña, Spain.

3 Institut de Génétique et de Biologie Moléculaire et Cellulaire, INSERM U 1258, CNRS UMR 7104, University of Strasbourg, 67404 Illkirch, France.

4 Platform for Metabolic Analyses, Structure Fédérative de Recherche Necker, INSERM US24/CNRS UAR 3633, Paris, France.

Corresponding author: Edor Kabashi edor.kabashi@institutimagine.org

Abstract

Background: Spinocerebellar ataxia type 36 (SCA36) is a late-onset neurodegenerative disorder caused by a GGCCTG hexanucleotide expansion in the first intron of *NOP56*. This mutation produces five dipeptide repeat proteins (DPRs) via repeat-associated non-ATG (RAN) translation, including poly-glycine-proline (poly-GP) which is the most abundant DPR in SCA36. However, the specific contribution of the poly-GP to SCA36 pathogenesis and the influence of NOP56 levels on poly-GP toxicity remains poorly understood.

Methods: We generated zebrafish models expressing poly-GP from an alternative codon sequence lacking the GGCCTG repeat, alone or in combination with partial *nop56* downregulation. Disease-associated phenotypes were evaluated by locomotor assays, immunostaining, apoptosis analysis and

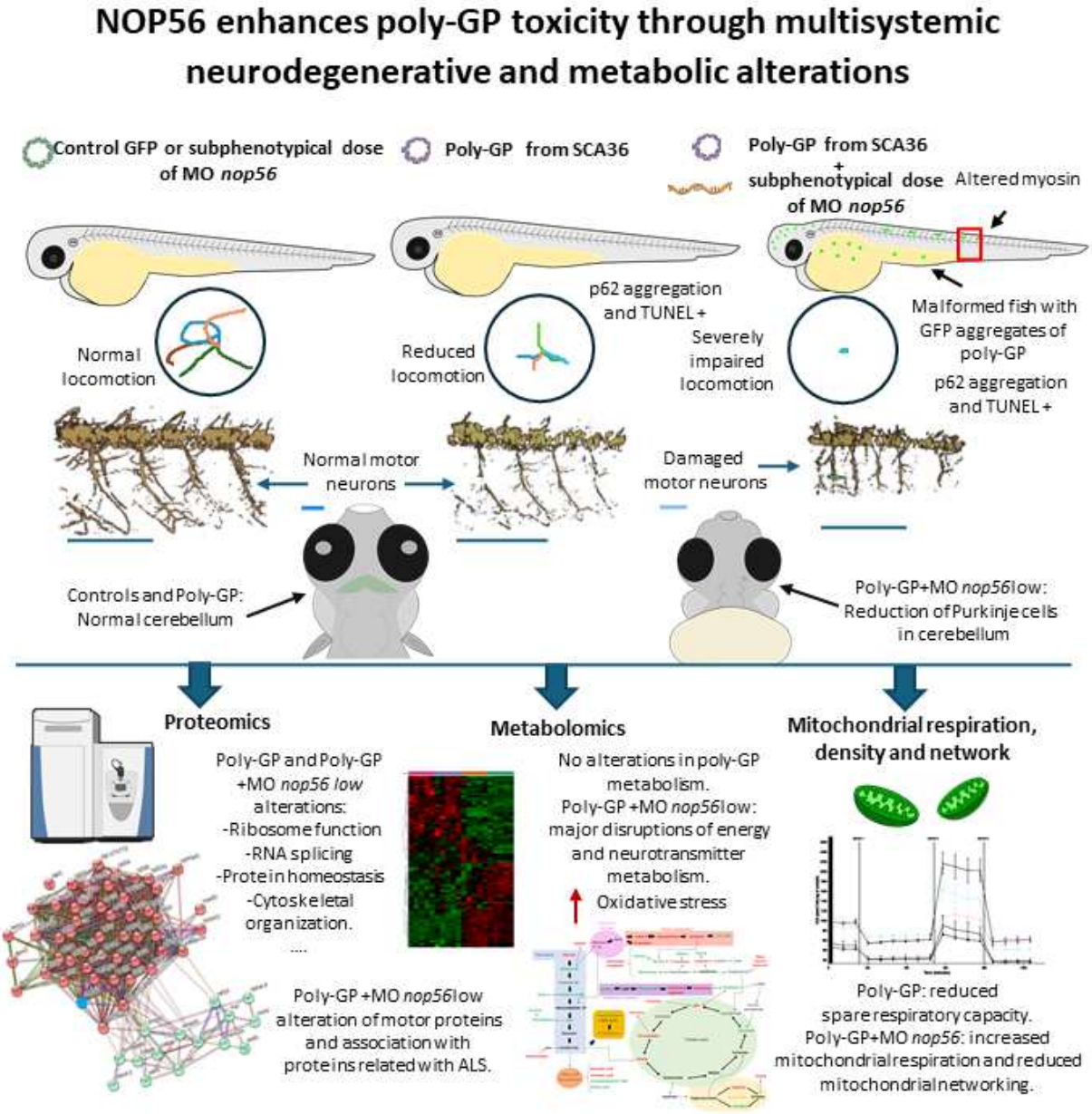
imaging of neuronal, muscular, and mitochondrial alterations. Proteomic and metabolomic profiling were performed to identify affected molecular pathways, followed by pathway enrichment analyses. Mitochondrial respiration was assessed using Seahorse analysis.

Results: Poly-GP expression alone induced locomotor impairment associated with p62 aggregation and increased TUNEL-positive cells. These phenotypes were exacerbated by partial *nop56* loss-of-function, which enhanced poly-GP accumulation and promoted cerebellar malformation, motor neuron defects, and myosin-associated muscle fiber dysfunction. Proteomic profiling identified convergent alterations in ribosomal function, protein homeostasis, and cytoskeletal organization in both models. Metabolomic analysis revealed extensive metabolic remodelling in the combined model, accompanied by increased mitochondrial respiratory activity. Notably, several of these molecular alterations overlap with pathways implicated in ALS and related neurodegenerative disorders, suggesting convergent pathogenic mechanisms.

Conclusions: Our findings demonstrate that partial *nop56* loss of function exacerbates poly-GP associated toxicity in the absence of repeat-derived RNA, supporting the hypothesis that alterations in *NOP56* expression influence the molecular response to DPR accumulation in SCA36. These results provide new insights into SCA36 pathogenesis and identify molecular and metabolic pathways that may inform future biomarker and therapeutic studies.

Keywords

SCA36, poly-GP, NOP56, dipeptide repeat proteins, repeat expansion disorders, neurodegeneration zebrafish.



Proteins and metabolites that could be potential biomarkers for SCA36 and other neurodegenerative diseases.

Background

Spinocerebellar ataxia type 36 (SCA36) is a late-onset dominant ataxia caused by atrophy of the cerebellum and its afferent and efferent connections. Its clinical phenotype includes gait impairment, hearing loss and motoneuronal dysfunction (most notably tongue atrophy and fasciculations, although limb involvement may also occur). The disease was first described in Japan, where it is known as "Asidan River ataxia" (1), and in Spain, known as "Ataxia da Costa da Morte" (2). SCA36 is caused by the GGCCTG expansion in the first intron of the *NOP56* gene. While healthy individuals typically carry

between 3 and 14 repeats, pathogenic expansions range from 30 to more than 2000 repeats. Interestingly, a similar intronic hexanucleotide repeat expansion (GGGGCC) in *C9ORF72* is the main cause of amyotrophic lateral sclerosis and frontotemporal dementia (C9 ALS/FTD) (3,4).

Current research into pathogenic mechanisms in SCA36 remains very limited, leaving the underlying mechanisms and molecular pathways largely unknown. There are discrepancies regarding the role of haploinsufficiency in the disease. Reduced *NOP56* expression has been reported in patients' peripheral blood and in iPSCs derived neurons (5,6), while increased *NOP56* expression has been observed in the region containing the expansion (intron 1–exon 2 junction) in the cerebellar cortex of patients (7). In zebrafish, *nop56* loss-of-function leads to severe neurodevelopmental defects, including absence of cerebellum, reduced number of 5HT interneurons, altered spinal motor neurons, locomotor deficits, increased apoptosis in the nervous system and premature death (8). Recently, a NOP56 knockout mouse model resulted in total embryonic lethality in homozygosity while heterozygous adult mice developed progressive cerebellar degeneration with Purkinje cell loss and impaired rotarod performance (9). These results suggest an essential role of *nop56* in nervous system development and maintenance and support a potential contribution of reduced *NOP56* gene dosage in SCA36 pathogenesis.

Repeats in SCA36 and C9 ALS/FTD undergo Repeat Associated Non-ATG (RAN) translation, being spontaneously translated without the need for a start codon or ATG, and producing dipeptide repeat proteins (DPRs) that accumulate in the nervous system (10–13). In SCA36, bidirectional translation across six different reading frames potentially produces five types of DPRs: poly-GL, poly-GP and poly-WA from the sense strand (5'-3'), and poly-GP, poly-AQ, poly-PR from the antisense strand (3'-5'). Among them, poly-PR and poly-GP are shared with C9 ALS/FTD (7,14,15). Poly-PR has been widely studied due to its high toxicity despite low abundance, whereas poly-GP has traditionally been considered less toxic. However, recent studies suggest that higher poly-GP levels correlate with more severe clinical phenotypes in C9 ALS/FTD patients (16), and poly-GP levels are reduced under antisense

oligonucleotide (ASO) BIIB078 treatment (17). In C9 ALS/FTD, TDP-43 pathology is present together with accumulation of stress granules and poly-GP inclusions that are p62 positive (7,18,19). In contrast, TDP-43 pathology or accumulation of stress granules has not been reported in SCA36 patient tissues. Although poly-GP is the most abundant DPR in SCA36, it remains soluble in brain tissue and does not associate with p62 in the frontal cortex and cerebellum (7), while some p62 positive inclusions were found in inferior olivary nucleus (20). Despite this evidence, the role of poly-GP in SCA36 neurodegeneration remains unclear and pathological mechanisms, potentially common between SCA36 and C9 ALS/FTD, remain largely unexplored.

Importantly, recent work in *Drosophila* models of SCA36 has demonstrated that neurotoxicity can arise from the combinatorial expression of repeat-associated RNA and dipeptide repeat proteins, including poly-GP, supporting a double hit model of SCA36 disease pathogenesis (21). Notably, poly-GP in this model has been reported to contribute significantly to neurotoxicity relative to other DPR species, highlighting its potential relevance in disease mechanisms.

Notably, in C9 ALS/FTD, *C9ORF72* loss-of-function, has been linked to autophagy defects leading to poly-GP accumulation and ultimately motor neuron apoptosis (22). This suggests that in C9 ALS/FTD, toxic gain-of-function and loss-of-function mechanisms may act synergistically. These findings raise the possibility that similar mechanisms could also contribute to SCA36 pathogenesis, which remains poorly understood.

Therefore, this work aims to investigate the interaction between poly-GP accumulation and reduced *nop56* function *in vivo* using zebrafish models, in which poly-GP is produced by canonical ATG-dependent translation from an alternative codon sequence, allowing its contribution to be examined independently of repeat-derived RNA and of the remaining DPRs. We show that poly-GP expression alone induces cellular dysfunction and functional alterations characterized by locomotor impairment, p62 aggregation, and increased TUNEL-positive cells, whereas *nop56* knockdown induces severe neurodegenerative defects consistent with previously described loss of function models (8).

Remarkably, subphenotypic *nop56* knockdown enhances poly-GP accumulation and toxicity, leading to cerebellar malformation, motor neuron defects and muscle dysfunction. By characterizing these effects at histopathological, locomotor, proteomic and metabolic levels, we identify convergent molecular mechanisms associated with neurodegeneration in SCA36, including pathways shared with ALS and related neurodegenerative disorders.

Methods

- **Zebrafish care and maintenance**

Zebrafish (*Danio rerio*) were maintained at the Institut Imagine fish facility (INSERM U1163, Paris, France) and bred in accordance with the National and European Guidelines for Animal Welfare (Directive 2010/63/EU). Experiments were performed on wild-type AB strain, heterozygous *nop56*^{sa12582} mutants obtained from the European Zebrafish Resource Center (EZRC), double transgenic line *Tg(mnx1:gal4)/Tg(UAS:RFP),* which expresses RFP specifically in motor neuron cell bodies and axons, and *Tg(actc1b:tomm20-ZsGreen),* in which expression of the Tomm20-ZsGreen fusion protein is driven by the muscle-specific α-actin (actc1b) promoter, resulting in ZsGreen labeling of mitochondria in muscle cells (23).

Fertilized eggs were collected after natural spawning. Zebrafish embryos and larvae were maintained in embryo medium (Instant Ocean, SS15-10) at 28ºC under a 14-h light/10-h dark cycle in a non-CO_2 incubator. Experimental procedures were approved by the National and Institutional Ethical Committees (code: 26775).

Embryos derived from a cross between *nop56*^{sa12582} heterozygous carriers and *Tg(mnx1:gal4)/Tg(UAS:RFP)* were genotyped at the end of the experimental procedures. Genomic DNA was released from individual embryos using the Phire Animal Tissue Direct PCR Kit (F140WH, Thermo Fisher Scientific; Waltham, USA) following the manufacturer's protocol. PCR was performed with Phire Hot Start II DNA Polymerase using the primers F: 5'-TGGCGGAAGATTTGATTCTG-3' and R: 5'-

TTTCCACTCGACATTCATCG-3', with an annealing temperature of 60 °C. PCR products were resolved on 1% agarose gels and genotypes were determined by Sanger sequencing on a 3730xl DNA Analyzer (Thermo Fisher Scientific). Sequences were analysed with CodonCode Aligner (CodonCode Corporation; Centerville, MA, USA)

- **Microinjections**

A GFP control plasmid and a poly-GP plasmid containing 100 glycine-proline repeats from an alternative codon sequence lacking the GGCCTG hexanucleotide repeat, preceded by an initiating ATG, flanked by an intron from *NOP56* human gene and fused to GFP (hereafter named SCA36-GP), were kindly provided by Dr Nicolas Charlet-Berguerand lab (IGBMC, Illkirch, France). Plasmids were microinjected at the DNA concentration of 100 ng/µl.

Morpholino antisense oligonucleotides (MO) were designed to bind the ATG start codon of zebrafish *nop56*: 5'ACGTGTAAAAGCACCATGTTTGCCG 3' Control MO, containing mismatch nucleotides with predicted binding sites in the zebrafish genome, has the following sequence: 5'-ATTCTCGAGCACAGCCTCAAGACAT-3' (Gene tools; Philomath, OR, USA). For loss-of-function modelling, embryos were injected with 0.3 mM of *nop56* MO (established as minimum effective dose). For combined loss and gain of function modelling we coinjected a subphenotypic dose of 0.15mM *nop56* MO along with 75ng/µl of SCA36-GP. Controls included coinjection of 100 ng/µl control GFP plasmid with 0.3 mM control MO (Cgfp+CMO) and injection of the subphenotypic dose of 0.15 mM *nop56* MO (MO*nop56*low). All the microinjections were carried out at one cell stage.

- **Imaging**

Embryos were screened for GFP fluorescence at 24 and 48 hours post fertilization (hpf) with a binocular fluorescence microscope (Olympus; Tokio, Japan). For live imaging, 48 hpf microinjected embryos from AB, *Tg(mnx1:gal4)/Tg(UAS:RFP)* or *Tg(actc1b:tomm20-ZsGreen)* lines were mounted in 1% low-melting-point agarose dissolved in embryo medium and supplemented with 0.16 mg/mL tricaine (A-

5040, Sigma-Aldrich; Saint Louis, USA). Images of the larvae general morphology, GFP aggregates, motor neurons and mitochondria were acquired using a Confocal Spinning Disk system (Carl Zeiss; Oberkochen, Germany) and a ZEISS Lightsheet 7 (Carl Zeiss) with 5x, 10x and 20x objectives.

For phenotypic characterization of larvae, three measurements were measured using Fiji software (Image J; National Institutes of Health; Bethesda, USA (24)): total length, head area, and eye area.

Axonal lengths of four ventral motor neuron projections were measured using Fiji software. Measurements were taken from the ventral root to the ventral edge of the musculature between 14th and 18th segments.

The density and level of organization (mitochondrial network index) of mitochondrial TOMM20-positive structures were analyzed using an in-house protocol developed for ImageJ or Fiji, which integrated FribrilTool, a plug-in published by (25) for the quantification of anisotropy.

- **Locomotion**

Locomotor phenotypes of 48 hpf zebrafish embryos were assessed using the Touched-Evoked Escape Response (TEER) test. In this assay, the tail of each embryo was mechanically stimulated with a tip to cause the stereotyped escape response to touch, which was recorded at 30 fps using a SpinView V2.0.0.147 software (FLIR Systems; Wilsonville, USA). Swimming trajectories were traced using the Manual Tracking plugin in ImageJ software, and distance and velocity were quantified.

- **Whole-mount immunohistochemistry and TUNEL staining**

Whole-mount immunohistochemistry was performed on 2 and 4 days post fertilization (dpf) zebrafish, using 10 fish per condition, following a previously established protocol (26). For TUNEL staining, we used 10 fish at 2 dpf following the manufacture's protocol of the "Click-iT™ Plus TUNEL Assay Kits for In Situ Apoptosis Detection, Alexa Fluor™ 647" (Thermo Fisher Scientific). For both protocols, embryos were treated with 0.003% 1-phenyl-2-thiourea (Sigma-Aldrich) at 24 hpf to prevent pigmentation. At 2dpf, zebrafish were anaesthetized with 0.16 mg/mL tricaine, fixed in 4% paraformaldehyde (Sigma-

Aldrich) for 2 h at room temperature (RT) and washed with PBS 3 times. Embryos were then dehydrated in methanol (Sigma-Aldrich) followed by gradual rehydration. After washes with PBST 0.1% and distilled water, they were permeabilized in fresh acetone (Sigma-Aldrich) for 20 min. Before starting subsequent steps, they were washed in distilled water and PBST.

For whole-mount immunohistochemistry, the samples were blocked in 10% bovine serum albumin (BSA; Eurobio Scientific; Les Ulis, France) diluted in 0.1% PBS Tween (0.1% PBST) for 2h at RT.

Primary antibodies diluted in 10% BSA were applied overnight at 4 °C: p62 (1:100 dilution; sc-28359, Santa Cruz Biotechnology; Dallas, USA), Zebrin II (1:100 dilution; mouse anti-Aldolase C; kindly provided by Prof. Richard Hawkes); F59 (1:10 dilution; Developmental Studies Hybridoma Bank - DSHB, Iowa, USA). Embryos then were washed in 0.1% PBST and incubated overnight at 4ºC with secondary antibodies diluted in 10% BSA: Alexa Fluor 488 and Alexa Fluor 568 (1:300 dilution; Thermo Fisher Scientific).

For both protocols, after additional PBS washes, embryos were mounted in 1% agarose in 50% glycerol and imaged using spinning disk system and ZEISS Lightsheet 7.

- **Western blot**

Pools of 30 zebrafish embryos at 48hpf were homogenized in RIPA buffer (50 mM Tris-HCl pH 7.5, 0.15 M NaCl, 0.5% Triton X-100) supplemented with protease inhibitors (Complete mini, 11836153001, Roche; Basel, Switzerland) by sonication. Lysates were centrifuged at maximum speed at 4ºC for 30 minutes and supernatants were collected. Protein concentration was calculated using a BCA assay (27). Proteins were denatured at 98°C for 5 minutes and 30 µg proteins per sample were separated by SDS polyacrylamide gel electrophoresis. Separated proteins were transferred to nitrocellulose membranes (1704270, Bio-Rad; Hercules, USA) and blocked in 0.5% milk in 0.1% PBST for 1h.

Primary antibodies diluted in blocking solution were applied overnight at 4ºC: poly(GP) TALS (1:20 dilution, DSHB) and β -actin (1:5000 dilution, 66009-1-Ig, Proteintech; Chicago, USA). After 0.1% PBST

washes, membranes were incubated with secondary antibodies (IRDye® 680RD and IRDye® 800CW Li-Cor; Lincoln, USA) diluted 1:5000 in blocking solution. Signals were detected using an ODYSSEY® CLx system (Li-Cor).

- **Statistical Analysis**

Data were analyzed and graphs generated using GraphPad Prism 9 (GraphPad; San Diego, USA (28)). Data normality was assessed using the D'Agostino–Pearson test. One-way analysis of variance (ANOVA), followed by Tukey's multiple comparison test, was performed, Statistical significance was established at p-value < 0.05.

- **Immunoprecipitation-based proteomic analysis**

To identify proteins associated with poly-GP, GFP-tagged poly-GP was immunoprecipitated using an anti-GFP antibody, and the immunoprecipitates were subjected to LC-MS/MS analysis. Therefore, proteomic analysis was restricted to conditions expressing the GFP-tag (Cgfp+CMO, SCA36-GP and SCA36-GP+ MO*nop56*low). 3 pools of 30 embryos of 48hpf per condition were used. Embryos were lysed in RIPA buffer (50 mM Tris-HCl pH 7.5, 0.15 M NaCl, 0.5% Triton X-100) supplemented with protease inhibitor cocktail (Sigma, 11873580001). Lysates were clarified by centrifugation at 14000 rpm for 30 min and supernatants were collected. GFP-tagged proteins were immunoprecipitated by incubating at 4°C for 1 h with pre-washed anti-GFP (Abcam, ab193983) Magnetic Beads in RIPA buffer. The beads were washed three times and then bound proteins were eluted by denaturation in Laemmli buffer at 95°C for 3 min. Protein mixtures precipitated with tricholoroacetic (TCA) overnight at 4°C, pellets were washed twice with 1 mL cold acetone, air-dried and resuspended in 2 M urea in 0.1 mM Tris-HCl pH 8.5 for reduction (5 mM TCEP, 30 min.) and alkylation (10 mM iodoacetamide, 30 min.). Trypsin digestion was carried out at 37°C overnight.

Extracted peptides were then analyzed using an Ultimate 3000 nano-RSLC (Thermo Fisher Scientific) coupled in line with either an Orbitrap ELITE or an Orbitrap Exploris 480 mass spectrometer (Thermo

Fisher Scientific) via a nano-electrospray ionization source equipped with the FAIMS Pro interface. Peptides were separated on a C18 Acclaim PepMap nano-column (75 µm ID x 25 cm, 2.6 µm, 150Å, Thermo Fisher Scientific) with a 20 minutes linear gradient from 8% to 35% buffer B (A: 0.1% formic acid (FA) in H_2O; B: 0.1% FA in 80% acetonitrile, flow rate 400 nl/min, 50°C) followed by a regeneration step at 90% buffer B and an equilibration at 8% buffer B. The total chromatography was 30 minutes. The mass spectrometer was operated in positive ionization mode in Data-Dependent Acquisition (DDA) with FAIMS compensation voltages (CV) of -45V. The DDA cycle consisted of one survey scans (350-1400 m/z, 90,000 FWHM) followed by MS^2 spectra (HCD; 30% normalized energy; 2 m/z window; 22,500 FWMH) in the limit of 1 sec. Unassigned and single charged states were rejected. Exclusion duration was set for 40 s with mass width was ± 10 ppm.

Proteins were identified with Proteome Discoverer 2.5 software (Thermo Fisher Scientific) and *Zebrafish* proteome database. Precursor and fragment mass tolerances were set at 10 ppm and 0.02 Da respectively, and up to 2 missed cleavages were allowed. Oxidation (M) and N-terminal Acetylation were set as variable modification, and Carbamidomethylation (C) as fixed modification. Peptides were filtered with a false discovery rate (FDR) at 1%, rank 1. Proteins were quantified with a minimum of 1 unique peptide based on the XIC (sum of the Extracted Ion Chromatogram). The quantification values were exported in Perseus (1.6.15.0) for statistical analysis involving a log[2] transform, imputation, normalization.

A Venn diagram was generated to compare both experimental conditions (Biovenn; https://www.biovenn.nl/index.php; (29). Pathway enrichment analysis was performed with ShinyGO 0.82 (https://bioinformatics.sdstate.edu/go/; (30) using a FDR cutoff of 0.05, minimum pathway size of 10 and maximum pathway size of 500. Pathways were selected based on FDR and sorted by fold enrichment. Protein interaction analysis of the enriched proteins was performed using the STRING database (https://string-db.org/; (31) with a minimum required interaction score of 0.7 (high confidence). Gene Set Enrichment Analysis was realized with Gestalt database (https://www.webgestalt.org/) with a minimum FDR score of 0.1.

- **Metabolomics**

For metabolomic analysis 5 pools of 10 embryos of 48hpf per condition were used. Metabolites were extracted using solution composed of 50% methanol, 30% acetonitrile (ACN) and 20% water. After addition of extraction solution, samples were vortexed for 5 min at 4 °C and centrifuged at 16,000 g for 15 min at 4 °C. The supernatants were collected and stored at −80 °C until analysis. LC/MS analyses were conducted on a QExactive Plus Orbitrap mass spectrometer equipped with an Ion Max source and a HESI II probe coupled to a Dionex UltiMate 3000 UPLC system (Thermo Fisher Scientific). The 5 µl samples were injected onto a SeQuant® ZIC®-HILIC Columns (150 mm × 2.1 mm; i.d. 5 µm) with a guard column (20 mm × 2.1 mm; i.d. 5 µm) (Millipore) for LC separation. Buffer A was 20 mM ammonium carbonate, 0.1% ammonium hydroxide (pH 9.2), and buffer B was ACN.

The chromatographic gradient was run at a flow rate of 0.2 µl min−1 as follows: 0–20 min, linear gradient from 80% to 20% of buffer B; 20–20.5 min, linear gradient from 20% to 80% of buffer B; 20.5–28 min, 80% buffer B. The mass spectrometer was operated in full scan, polarity switching mode with the spray voltage set to 2.5 kV and the heated capillary held at 320 °C. The sheath gas flow was set to 20 units, the auxiliary gas flow to 5 units and the sweep gas flow to 0 units. The metabolites were detected across a mass range of 75–1000 m/z at a resolution of 35,000 (at 200 m/z) with the automatic gain control target at 106 and the maximum injection time at 250 ms. Lock masses were used to ensure mass accuracy below 5 ppm. Data were acquired with Thermo Xcalibur software (Thermo Fisher Scientific). The peak area of metabolites was determined using Thermo TraceFinder software (Thermo Fisher Scientific), identified by the exact mass of each singly charged ion and by the known retention time on the HPLC column.

Metabolomic data were normalized and a student-t test was performed using MetaboAnalyst 6.0 (https://www.metaboanalyst.ca/; (32)). Significant data were filter using the following criteria: $p < 0.05$, fold change > 1.5, VIP score > 1. Pathway enrichment analysis was performed according to the

KEGG database and RaMP-DB which integrate KEGG pathways via HMDB, Reactome, WikiPathways. A Venn diagram was generated to compare both experimental conditions (Biovenn).

Finally, an integrative analysis of significant metabolomics and proteomics data was performed in MetaboAnalyst 6.0 using Joint Pathway Analysis. Pathway impact values > 0.20 were considered significant.

- **Seahorse**

48hpf zebrafish embryos were euthanized with 0.3 mg/mL tricaine and dissociated with 0.25% EDTA-trypsin at 30°C by pipetting up and down during 1h. Digestion was stopped with 10% fetal calf serum and cells were centrifuged at 600 rpm for 6 minutes at room temperature and resuspended in sodium bicarbonate ($NaHCO_3$)-free DMEM. Cell concentration was determined using an automated cell counter. Cells were plated in 96-well plates using 300.000 cells per well with at least 4 wells per condition and incubated for 1 hour at 28º C. Mitochondrial stress tests were conducted using the Seahorse XFe96 Analyzer (Agilent Technologies; Santa Clara, USA) at 28 °C, following the manufacturer's protocol.

The oxygen consumption rate (OCR) was measured under basal conditions and subsequently after sequential injections of oligomycin (4 µM), fluorocarbonyl cyanide phenylhydrazone (FCCP; 4 µM), and a combination of rotenone and antimycin A (6 µM). Oligomycin-sensitive OCR reflects ATP-linked respiration, while FCCP-induced OCR indicates the maximal mitochondrial respiratory capacity. The final injection of rotenone/antimycin A was used to determine non-mitochondrial respiration.

Raw OCR data were normalized to total protein content per well to account for variability in cell number and ensure accurate comparisons across samples. Student-t test was considered significant with $p < 0.05$ and graphs were generated with Agilent Seahorse Analytics.

Results

- **Nop56 knockdown enhances poly-GP accumulation, causes malformations and p62 aggregation**

In vivo poly-GP accumulation in SCA36 was modeled by injecting a construct containing 100 poly-GP repeats downstream of an intronic human sequence of the *NOP56* gene fused to a GFP tag (referred to as "SCA36-GP") into one-cell stage zebrafish embryos (Fig 1A). Loss of function was modeled by knocking down the zebrafish *nop56* homolog (ENSDART00000114524.5) using a translation-blocking morpholino. We determined that the lowest dose causing a phenotype was 0.3 mM ("MO*nop56*" group), while we determined that 0.15 mM was a subphenotypic dose that did not cause any detectable neurodegenerative phenotype or morphological abnormalities in zebrafish embryos ("MO*nop56*low") (Supplementary figure 1). A combined model of poly-GP and partial knockdown of *nop56* function was generated by co-injecting SCA36-GP plasmid with the subphenotypic dose of the *nop56* morpholino ("SCA36-GP+ MO*nop56*low" group). As control, a GFP plasmid was co-injected with a mismatch morpholino ("Cgfp+CMO") (Fig 1A).

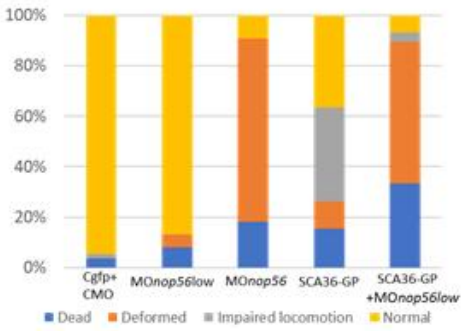
MO*nop56* and SCA36-GP+MO*nop56*low groups showed increased embryonic lethality and morphological malformations resembling the previously described *nop56* loss-of-function model (8), including reduced body size and curvature, abnormal eye morphology, swollen yolk, cardiac edema, head malformations, and impaired locomotion. However, in SCA36-GP only 10% of embryos displayed macroscopic defects, with 10% increase in lethality, but 40% of morphologically normal embryos showed reduced locomotion (Fig 1B). No morphological or locomotor defects were observed in MO*nop56*low or controls (Fig 1B). Poly-GP was detected in SCA36-GP and SCA36-GP+MO*nop56*low embryos by Western blot at 48 hpf at the expected size of 70KDa (Fig 1C), with stronger accumulation in the combined model.

Poly-GP inclusions were detected at 24 hpf based on GFP fluorescence in both models injected with the SCA36-GP plasmid. In SCA36-GP embryos, inclusions were rapidly cleared, with almost no fluorescence remaining at 48 hpf (Fig 1D). In contrast, in SCA36-GP+MO*nop56*low embryos, aggregates accumulated at 48 hpf (Fig 1D) and can be seen in different regions of the embryo. This different presence of poly-GP aggregates at 48hpf is consistent with the western blot findings. To test whether poly-GP accumulation was associated with alterations in autophagy, we performed immunofluorescence using an anti-p62 antibody at 3dpf. p62 positive aggregates were detected in both SCA36-GP and SCA36-GP+MO*nop56*low predominantly in the head and skeletal muscle. No accumulation was observed in control or MO*nop56* embryos, indicating that altered autophagy is associated with poly-GP (Fig 1G).

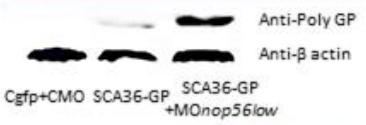
A

Injection	Concentration	Phenotype
Control GFP +Control MO	100ng/µl + 0.3 mM	Non phenotypic
MO *nop56low*	0.15 mM	Non phenotypic
MO *nop56*	0.3 mM	Malformations, Impaired locomotion
SCA36-GP	100ng/µl	Impaired locomotion
SCA36-GP+ MO *nop56* low	75 ng/µl+ 0.15 mM	Malformations, Impaired locomotion

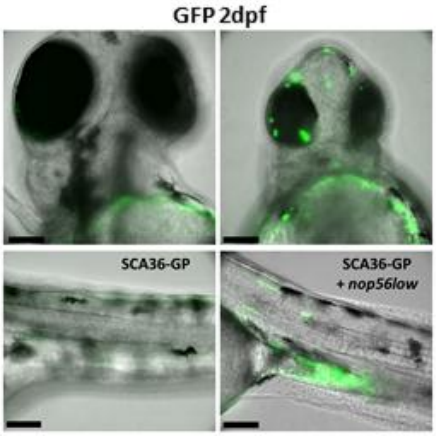
B



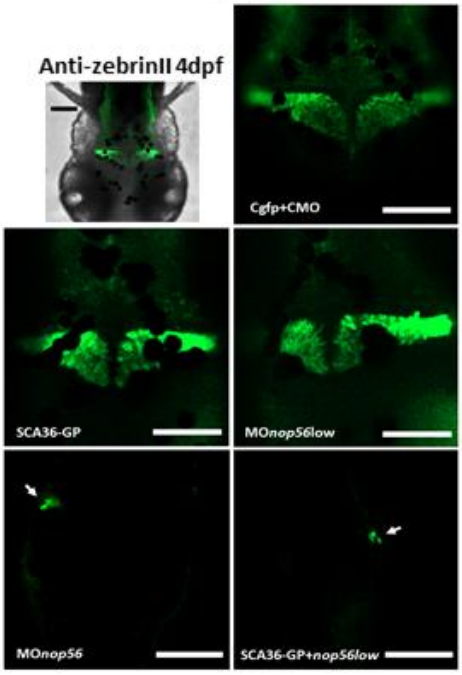
C

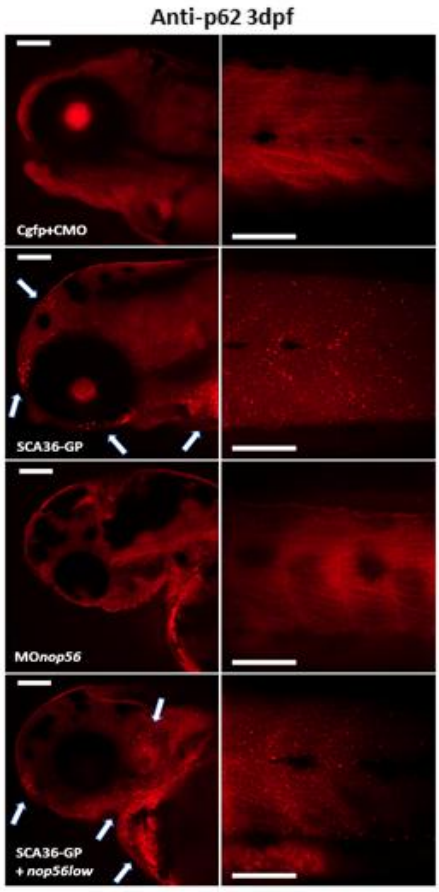


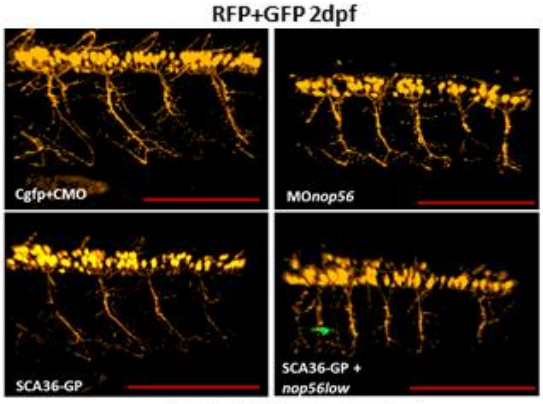
D



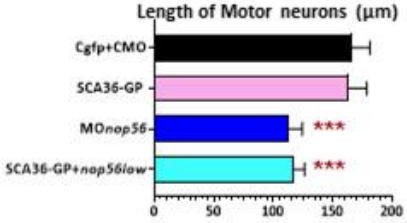
E







F



G

330

Figure 1. Characterization of molecular mechanisms of SCA36 in zebrafish embryos. A. Scheme of the different experimental groups, doses and observed phenotypes. B. Graph with proportion of embryos that were dead, deformed or morphologically normal in each condition at 48 hpf. For normal embryos, proportion that displayed locomotor defects is shown. C. Anti-poly GP Western blot revealing higher accumulation of poly-GP under *nop56* knockdown at 48hpf. Poly-GP band appears at 70KDa, while β actin at 42 KDa. D. GFP fluorescence revealing poly-GP aggregates in the head and tail of SCA36-GP+ MO*nop56*low embryos but not in SCA36-GP at 48hpf. Scale bars: 100µm. E. Expression of Zebrin II (green) in Purkinje cells of the cerebellum at 4dpf. Note the marked malformation of the cerebellum in MO*nop56* and SCA36-GP+ MO*nop56* groups, with the presence of only very few Purkinje cells (white arrows). Scale bars: 100µm F. Imaging of motor neurons in *Tg(mnx1:gal4)/Tg(UAS:RFP)* line at 2dpf showed that MO*nop56* and in SCA36-GP+ MO*nop56* embryos display reduced abnormal axon length and branching, as well as decreased number of motor cell bodies. A green poly-GP aggregate is also visible in SCA36-GP+ MO*nop56*low. Scale bars: 200µm. Motor neuron length data are presented as mean + standard error of the mean (SEM). Significance indicated with * $p < 0.05$, $p < 0.01$ or *** $p < 0.001$. G. Anti-p62 immunofluorescence showing accumulation of p62 aggregates (red, marked by white arrows) in SCA36-GP and SCA36-GP+ MO*nop56*low embryos at 3dpf, suggesting autophagy alteration. Scale bars: 100µm.**

- **SCA36 zebrafish models display neurodevelopmental and neuromuscular defects**

To investigate central nervous system abnormalities, we performed zebrin II immunostaining at 4 dpf. Both MO*nop56* and SCA36-GP+MO*nop56*low embryos lacked a fully formed cerebellum and displayed only a few Purkinje cells (Fig 1E). In contrast, control, SCA36-GP and MO*nop56*low embryos had a normal cerebellum (Fig 1E). Analysis of motor neurons in *Tg(mnx1:gal4)/Tg(UAS:RFP)* line at 2dpf revealed reduced axon length and decreased number of cell bodies in MO*nop56* and in SCA36-GP+MO*nop56*low embryos (Fig 1F). The combined model also showed reduced axonal branching (Fig 1F). No alterations in motor neurons were observed in controls or SCA36-GP.

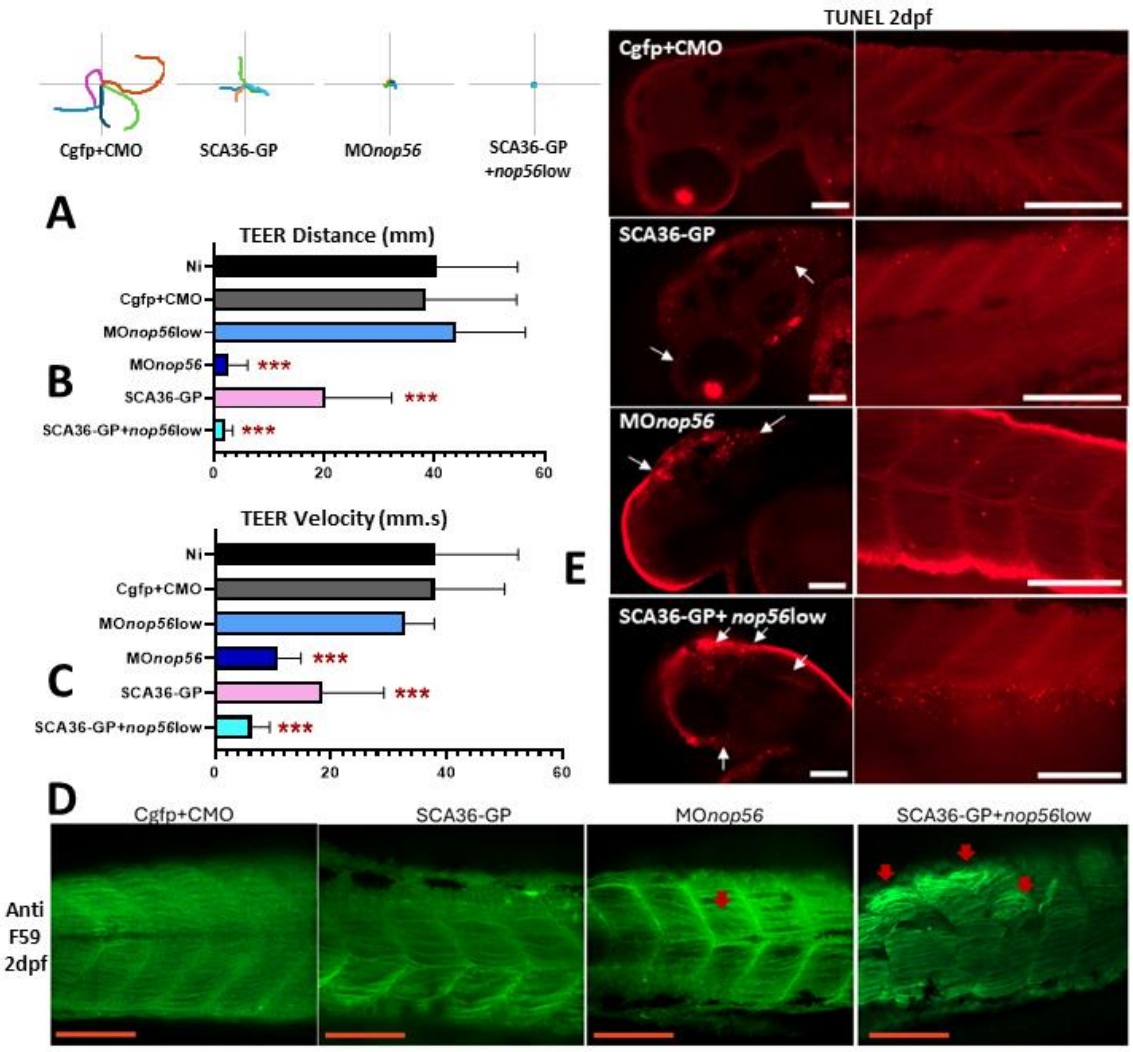


Figure 2. Locomotor and muscular defects in SCA36 zebrafish models. A-C TEER analysis at 48hpf showed significant reduction in total distance travelled and velocity in SCA36-GP, MO*nop56* and SCA36-GP+ MO*nop56*low groups. A. representative tracks of 5 fish per condition. B-C Data are presented as mean + standard error of the mean (SEM). Significance indicated with * $p < 0.05$, $p < 0.01$ or *** $p < 0.001$. D. Myosin heavy chain immunostaining using F59 antibody at 2dpf showed disorganized fibers (red arrows). Scale bars: 100 µm. E. TUNEL staining revealed increased apoptosis in the head and muscle of SCA36-GP, MO*nop56*, and SCA36-GP+MO*nop56*low embryos. Scale bars: 100 µm.**

Locomotion was quantified at 48 hpf using Touch-Evoked Escape Response (TEER) analysis, which reveals stereotyped escape responses to touch permitting an assessment of motor ability. Non injected control embryos (Ni), control and MO*nop56*low embryos showed no significant differences in distance

covered or velocity (Fig 2A-C). In contrast, SCA36-GP embryos exhibited moderately reduced locomotion, while MO*nop56* and SCA36-GP+ MO*nop56*low showed severe paralysis (Fig 2A-C).

To assess whether locomotor defects were associated with myosin abnormalities, we performed immunostaining with F59 (myosin heavy chain) antibody at 2dpf (Fig 2D). SCA36-GP embryos showed no differences compared to controls. Conversely, MO*nop56* and SCA36-GP+MO*nop56*low embryos exhibited disorganization of heavy chain fibers, more severe in the combined model. These results suggest that locomotor defects in MO*nop56* and SCA36-GP+MO*nop56*low embryos may be associated with structural alterations affecting muscle fibers, motor neurons and cerebellar development. In contrast, no structural alterations were detected in these tissues in SCA36-GP, suggesting that their locomotor impairment may instead arise from more subtle cellular dysfunction, not being associated with overt myofiber damage at this stage.

Moreover, TUNEL staining revealed increased apoptosis in the head region of SCA36-GP, MO*nop56*, and SCA36-GP+MO*nop56*low embryos (Fig 2E). Apoptotic cells were also detected in the muscle across all three conditions, although to a lesser extent in SCA36-GP embryos (Fig 2E). Notably, apoptosis was also observed in the notochord of SCA36-GP+MO*nop56*low embryos. These findings suggest that both poly-GP expression and *nop56* reduction promote cellular vulnerability and cell death-associated phenotypes, with a more severe and widespread effect in the combined condition.

- **Poly-GP also accumulates in *nop56* heterozygous embryos, causing motor neuron and locomotor defects**

Given that there is a higher accumulation poly-GP after partial reduction of *nop56*, we investigated whether a similar effect occurs in heterozygous fish of the *nop56*^{sa12582} knockout line (8). For this purpose, SCA36-GP was injected into wild type AB embryos ("SCA36-GP (WT)") and in embryos obtained from *nop56*$^{+/-}$ incross ("SCA36-GP (*nop56*$^{+/-}$)"). In the latter group, we observed that

approximately 50% of the injected embryos, corresponding with *nop56*$^{+/-}$, displayed enhanced poly-GP accumulation in the head at 48 hpf, without showing gross morphological abnormalities. Moreover, motor neurons in SCA36-GP (*nop56*$^{+/-}$) embryos exhibited reduced branching and shorter axons (Fig 3A-B). Locomotion was significantly decreased in both SCA36-GP models compared to control, with SCA36-GP (*nop56*$^{+/-}$) showing a more pronounced reduction than SCA36-GP (WT). These findings suggest that *nop56* heterozygosity enhances poly-GP accumulation and exacerbates motor neuron and locomotor defects, like the SCA36-GP+MO*nop56*low combined model, but without inducing gross morphological abnormalities.

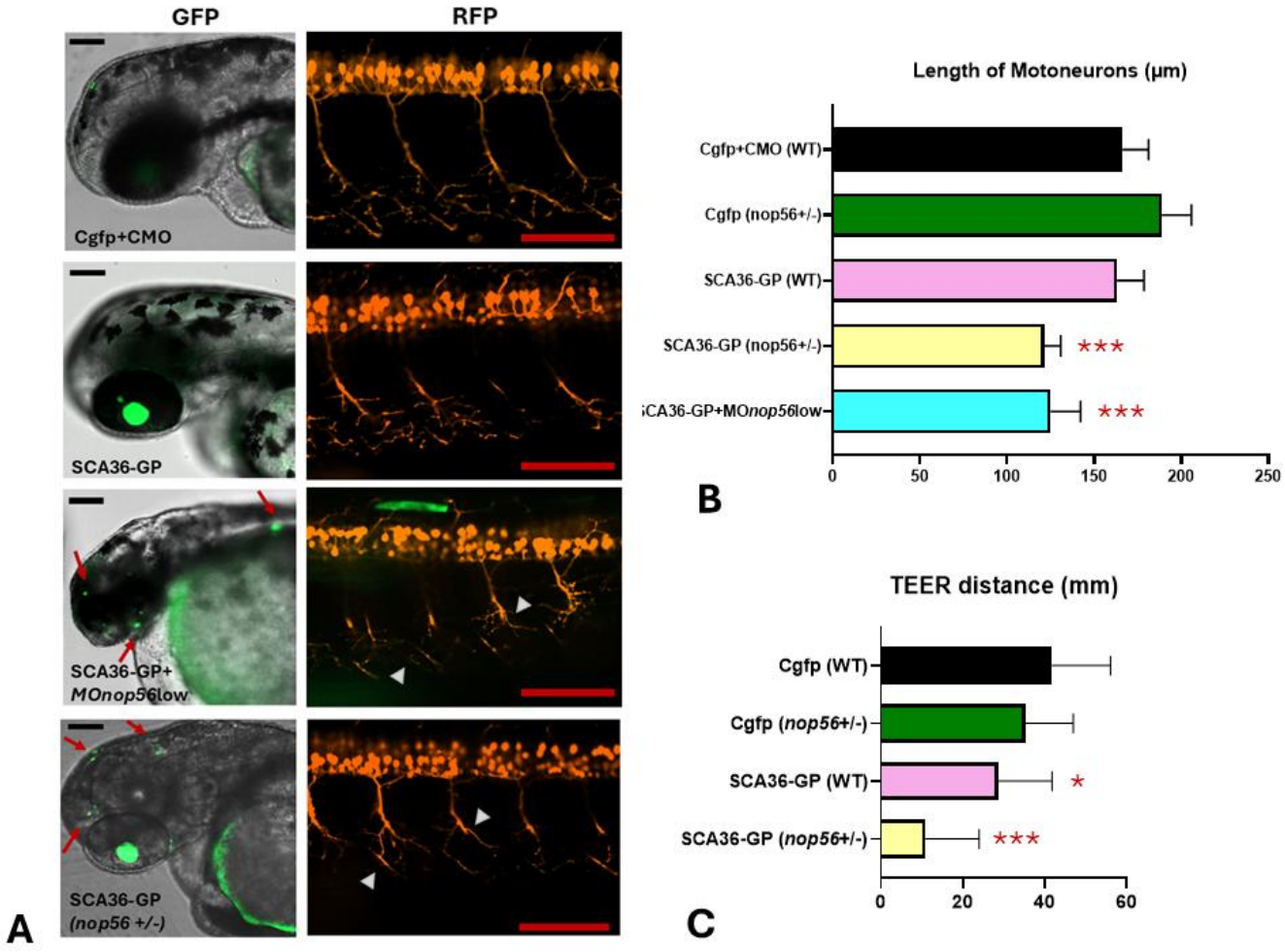


Figure 3. Injection of SCA36-GP in *nop56*$^{+/-}$ embryos leads to poly-GP accumulation and motor neuron defects. A-B. Poly-GP aggregates (red arrows) and motor neurons with reduced branching and shorter axons are observed at 2 dpf (white arrows). Scale bars: 100µm. C. TEER analysis showing significantly reduced locomotor distance in both SCA36-GP (WT) and

SCA36-GP (*nop56*$^{+/-}$) with a more pronounced effect in *nop56*$^{+/-}$. Data are presented as mean + standard error of the mean (SEM). Significance indicated with * p < 0.05, p < 0.01 or *** p < 0.001.**

- **Proteomic analysis reveals differential pathway enrichment in SCA36-GP and SCA36-GP+MO*nop56*low zebrafish models**

Proteomic analysis of GFP-immunoprecipitated protein complexes identified a total of 607 proteins across all samples. Among these, 183 proteins were differentially abundant in SCA36-GP compared to the control group (116 enriched and 67 depleted). Partial *nop56* depletion markedly enhanced the proteomic alterations induced by poly-GP expression, with 280 proteins differentially abundant in the SCA36-GP+MO*nop56*low group compared to control (142 enriched and 138 depleted) (Supplementary Table 1). Principal component analysis (PCA) demonstrated clear separation between control, SCA36-GP, and SCA36-GP+MO*nop56*low samples, indicating distinct protein enrichment profiles for the three experimental groups (Fig 4A).

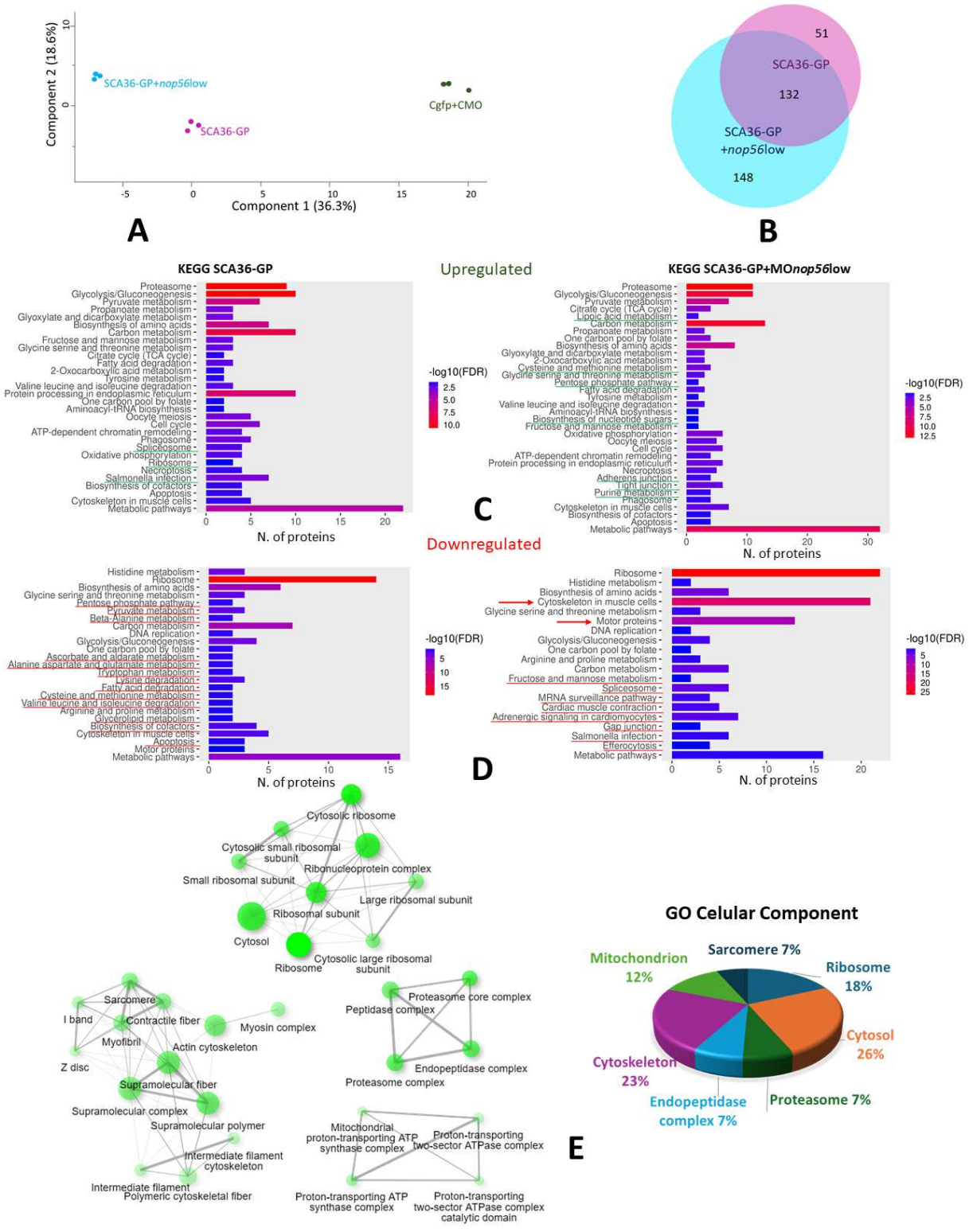
Comparison of the SCA36-GP and SCA36-GP+MO*nop56*low datasets revealed a shared set of 132 differentially abundant proteins relative to controls (Fig 4B). Functional enrichment analysis revealed that these shared proteins were mainly associated with KEGG pathways related to ribosome biogenesis spliceosome, proteasome, metabolism, oxidative phosphorylation and muscle cytoskeleton, among others (Fig 4C-D). Despite this overlap, partial *nop56* depletion substantially expanded the proteosome alterations, with 148 proteins uniquely altered in the SCA36-GP+MO*nop56*low group compared with only 51 proteins specific to SCA36-GP. Thus, SCA36-GP alone displayed a more restricted proteomic response, with predominance of ribosome and metabolic pathways.

SCA36-GP+MO*nop56*low showed a stronger depletion of proteins involved in ribosome function, RNA splicing and mRNA surveillance. In addition, this condition presented a stronger reduction in motor proteins and muscle cytoskeleton components, together with selective decrease in proteins involved in cardiac muscle contraction, adrenergic signalling in cardiomyocytes, and gap junctions. Although

apoptosis-related pathways were identified in both models, proteins related with these pathways were selectively reduced in the SCA36-GP group (Fig 4C-D).

To independently validate the pathway enrichment results, we performed preranked Gene Set Enrichment Analysis (GSEA) using all quantified proteins ranked by log2 fold change. KEGG-based GSEA confirmed significant positive enrichment of proteasome-related pathways and negative enrichment of ribosome pathways in the SCA36-GP model. Similarly, in the combined SCA36-GP+MO*nop56*low model, KEGG-based GSEA also confirmed enrichment of proteasome-related pathways and depletion of ribosome pathways. In addition, the combined model also showed enrichment of lysosome, autophagy and apoptosis pathways, together with depletion of motor protein-related pathways (Supplementary figure 2). Reactome-based GSEA further supported these findings, revealing repression of rRNA processing, translation and nonsense-mediated decay in both models, together with coordinated activation of immune, DNA damage, apoptotic and metabolic pathways. In addition, compared with SCA36-GP, the combined model showed stronger enrichment of cell cycle and signal transduction pathways, and reduction of muscle contraction pathways (Supplementary figure 2).

Gene Ontology (GO) Cellular Component analysis showed that differentially abundant proteins in the SCA36-GP+MO*nop56*low group were mainly associated with the ribosome, proteasome, endopeptidase complex, cytosol, cytoskeleton and sarcomere, and mitochondria (Fig. 4E). A similar distribution was observed in the SCA36-GP group (data not shown).



445

446 **Figure 4. Proteomic analysis of GFP-immunoprecipitated protein complexes obtained from Cgfp+CMO, SCA36-GP and**
447 **SCA36-GP+MO*nop56*low embryos. A. Principal component analysis (PCA) showing the separation of proteomic profiles**
448 **among experimental groups. B. Venn diagram showing the overlap of differentially abundant proteins between SCA36-GP**
449 **and SCA36-GP+MO*nop56*low relative to controls. A total of 132 proteins were shared between both groups, while 51 and**

148 proteins were exclusively altered in the SCA36-GP and SCA36-GP+MO*nop56*low groups, respectively. C-D. KEGG pathway enrichment analysis of enriched (C) and depleted (D) proteins in SCA36-GP and SCA36-GP+MO*nop56*low groups in comparison with control. Only significantly altered pathways are shown (selected based on FDR<0.05 and sorted by fold enrichment). Pathways that differ between the two groups are underlined. In D, the *cytoskeleton in muscle cells* and *motor proteins* pathways contained substantially more altered proteins in SCA36-GP+MO*nop56*low than in SCA36-GP, as indicated by the arrow. E. GO Cellular Component enrichment analysis. The left panel shows the distribution network of the top 30 of differentially abundant proteins in SCA36-GP+MO*nop56*low relative to control. The right panel shows a pie chart summarizing the distribution of the main enriched cellular components. A similar GO Cellular Component distribution was observed for SCA36-GP (data not shown). All enrichment analyses were performed using ShinyGO v0.85.

To further characterize the molecular pathways underlying the proteomic changes, we examined selected proteins with potential functional relevance. Ribosomal and spliceosomal proteins were predominantly depleted in both SCA36-GP and SCA36-GP+MO*nop56*low groups with a more pronounced reduction in the combined model (Fig 5A-B). Proteosomal proteins were significantly enriched in both groups (Fig 5C).

Motor proteins also showed a marked reduction in abundance in SCA36-GP+MO*nop56*low embryos (Fig 5D), in agreement with the motor myosin abnormalities reported before. Moreover, several proteins associated with central nervous system function were particularly affected in the SCA36-GP+MO*nop56*low group, including Camk2g1 (involved in synapse formation and synaptic plasticity), Mapta (encoding the microtubule-associated protein tau), and Smndc1 (spliceosome component linked to motor neuron survival) (Fig 5E). In addition, we found altered proteins related to neuropeptides: Npepps, an aminopeptidase involved in neuropeptide regulation and has been linked previously linked to tauopathies, was significantly depleted only in the SCA36-GP+MO*nop56*low group, whereas Thop1, a neuropeptidase implicated in neuropeptide degradation and amyloid-beta precursor protein processing, was significantly enriched in this group (Fig 5F).

Proteins involved in mitochondrial respiration were also differentially associated in both SCA36-GP and SCA36-GP+MO*nop56*low groups (Fig 5G). Interestingly, several proteins associated with ALS also

displayed altered abundance (Fig 5H). Fus and Sod1 were significantly depleted in both SCA36-GP and SCA36-GP+MO*nop56*low groups, whereas Taf15 was selectively reduced in the combined model. STRING network analysis revealed that ribosomal proteins, including Nop56, formed a highly interconnected network with RNA-binding and splicing-related proteins, including Fus, Sod1, Taf15, and Hnrnpa1b, many of which are linked to ALS pathophysiology (Fig 5H).

Together, these findings showed that SCA36 poly-GP expression induces widespread remodelling of ribosome function, RNA metabolism, proteostasis, and metabolic pathways, while partial *nop*56 depletion exacerbates these alterations and promotes additional defects in cytoskeletal organization and neuronal homeostasis.

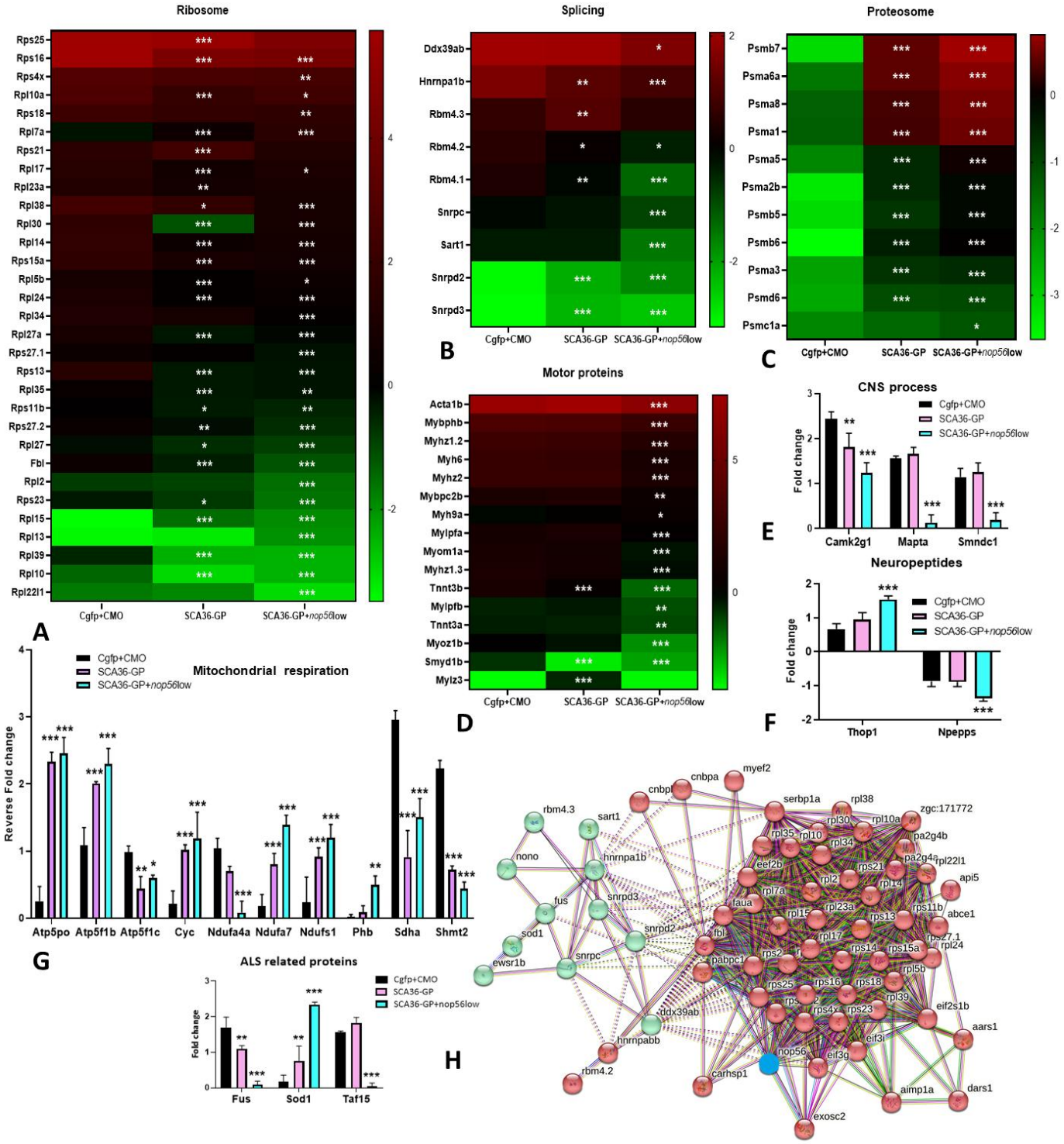
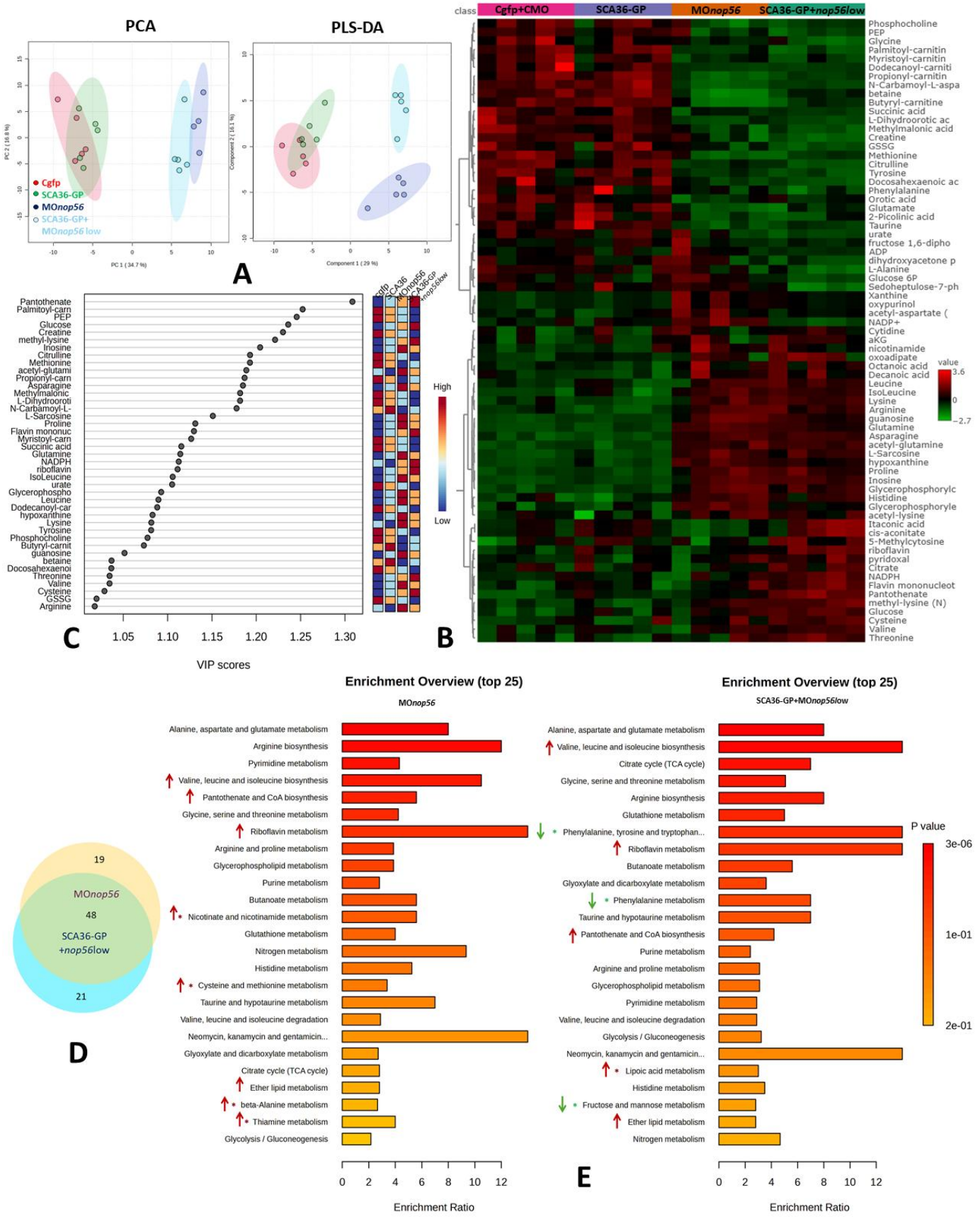


Figure 5. Heatmaps showing the fold change of selected proteins which significant increase (red) or decrease (green) abundance related with ribosome (A), proteosome (B), RNA splicing (C) and motor proteins (D). Significance indicated with * p < 0.05, p < 0.01 or *** p < 0.001. E. Differential abundance of most relevant proteins associated with CNS processes in SCA36-GP+MO*nop56*low group. F. Differential abundance of proteins that regulate neuropeptide activity and metabolism in SCA36-GP+MO*nop56*low. G. Mitochondrial respiratory chain associated proteins also show significant differential abundance in SCA36-GP+MO*nop56l*ow. H. Differential abundance of ALS-associated proteins (left) and STRING**

network analysis (right). Fus and Sod1 showed significant differential abundance in both SCA36-GP+MO*nop56*low and SCA36-GP, while Taf15 that is depleted only in SCA36-GP+MO*nop56*low. STRING protein–protein interaction analysis of proteins showing significant differential association identified a highly connected network enriched in proteins involved in ribosome function (red), a functional group to which NOP56 belongs (blue). This network was connected to proteins involved in RNA binding and splicing (green), including proteins associated with ALS Data are presented as mean + standard error of the mean (SEM). Significance indicated with * p < 0.05, p < 0.01 or *** p < 0.001.**

- **Widespread remodelling of metabolic pathways in SCA36-GP+MO*nop56*low**

As proteomic analysis revealed extensive alterations in metabolic pathways, we next performed metabolomic profiling to determine whether these changes were reflected at the metabolite level. To distinguish metabolic alterations associated with Poly-GP expression from those associated with *nop56* downregulation, MO*nop56* embryos were analyzed in addition to SCA36-GP and SCA36-GP+MO*nop56*low. Metabolomic analysis detected 144 metabolites, of which 70 showed significant alterations in SCA36-GP+MO*nop56*low group compared with control (38 upregulated and 32 downregulated), 68 in MO*nop56* group (46 upregulated, 22 downregulated) and 3 in the SCA36-GP group (all upregulated) (Supplementary Table 2). PCA and Partial Least-Squares Discriminant Analysis (PLS-DA) showed minimal separation between SCA36-GP and control, suggesting limited metabolic differences between these groups. In contrast, MO*nop56* and SCA36-GP+MO*nop56*low exhibited clear clustering, suggesting distinct metabolic profiles compared with the other two groups (Fig 6A). Heatmaps and VIP score analysis revealed key metabolites, including pantothenate, diverse acylcarnitines, acetyl-glutamine, inosine, methionine, glutamine, glutamate, glucose, creatine and glycine, among others (Fig 6B-C).



516

517 **Figure 6. A. PCA and PLS-DA plots of the metabolomic samples. B. Heatmap of the 71 metabolites significant altered in the**

518 **SCA36-GP+MO*nop56*low group. Red indicates upregulation, green indicates downregulation. C. VIP score >1 highlighting**

the most relevant metabolites. D. Venn diagram showing the overlap of 48 significantly altered metabolites between MO*nop56* and SCA36-GP+MO*nop56*low groups relative to controls, 19 metabolites unique to MO*nop56* group and 21 metabolites unique to SCA36-GP+MO*nop56*low group. E. Top 25 KEGG pathways enriched in SCA36-GP+MO*nop56*low and MO*nop56*. Pathways unique in these groups are indicated with a *, reds arrows indicate upregulation and green arrows indicated downregulation. A-C and E Images generated using MetaboAnalyst.

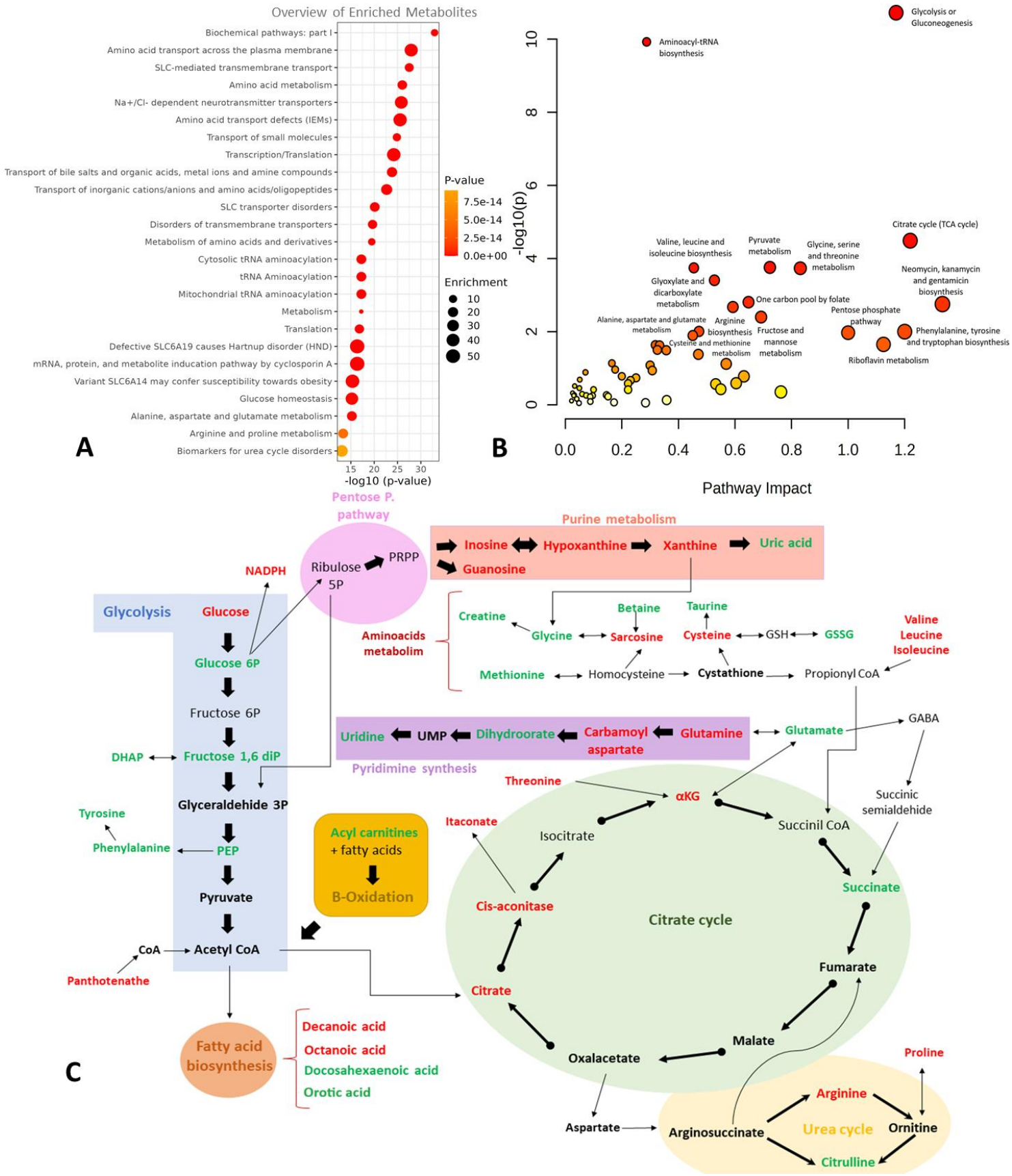
In SCA36-GP group, the only significantly altered metabolites were guanosine (also altered in MO*nop56* and SCA36-GP+MO*nop56*low), oxaloacetic acid and glycerol. These data indicate that poly-GP expression alone induces only limited metabolic changes. In contrast, MO*nop56* and SCA36-GP+MO*nop56*low shared 48 altered metabolites, while 19 and 21 metabolites, respectively, were exclusively altered in each condition relative to control (Fig 6D).

KEGG enrichment analysis revealed a similar metabolic profile in MO*nop56* and SCA36-GP+MO*nop56*low. Both conditions showed enrichment of pathways, involved in amino acid metabolism, nucleotide, cofactor and lipid metabolism. Several of these pathways contained both up and downregulated metabolites, indicating extensive metabolic reorganization. Despite these similarities, pathway enrichment highlighted distinct metabolic features in each condition. Pathways related to nitrogen and amino acid metabolism, including “arginine biosynthesis” and “histidine metabolism”, were more prominent in MO*nop56*, together with exclusive enrichment of “nicotinate and nicotinamide metabolism”, “cysteine and methionine metabolism”, “beta-alanine metabolism”, and “thiamine metabolism”. In contrast, SCA36-GP+MO*nop56*low showed stronger enrichment of central carbon and amino acid metabolism showing exclusive downregulation of “phenylalanine, tyrosine and tryptophan metabolism”, “phenylalanine metabolism”, “fructose and mannose metabolism”, together with exclusive upregulation of “lipoic acid metabolism” (Fig. 6E).

Overall, these findings indicate that strong *nop56* knockdown is sufficient to induce extensive metabolic remodelling, which is largely recapitulated in the SCA36-GP+MO*nop56*low condition particularly affecting central carbon and amino acid metabolism, suggesting that poly-GP selectively

545 modifies the metabolic consequences of *nop56* reduction. Therefore, subsequent integrative pathway
546 analyses focused on the combined model, to further investigate the interaction between *nop56*
547 deficiency and poly-GP accumulation.

548 RaMP-DB analysis that integrates KEGG pathways via HMDB, Reactome, WikiPathways in SCA36-
549 GP+MO*nop56l*ow group indicated major alterations in the process: “SLC mediated membrane
550 transport”, “disorders of transmembrane transport”, “Na^+/Cl^- dependent neurotransmitter”, “amino
551 acid metabolism”, “transcription/translation”, “cytosolic and mitochondrial tRNA aminoacylation”,
552 “glucose homeostasis” and “alanine, aspartate and glutamate metabolism” (Fig 7A).



553 **Figure 7. A. RaMP-DB analysis in SCA36-GP+MO*nop56*low. B. Integrated analysis of the proteomic and metabolomic**

554 **pathways more altered. A-B graphs generated using MetaboAnalyst. C. Metabolic map of the most significantly altered**

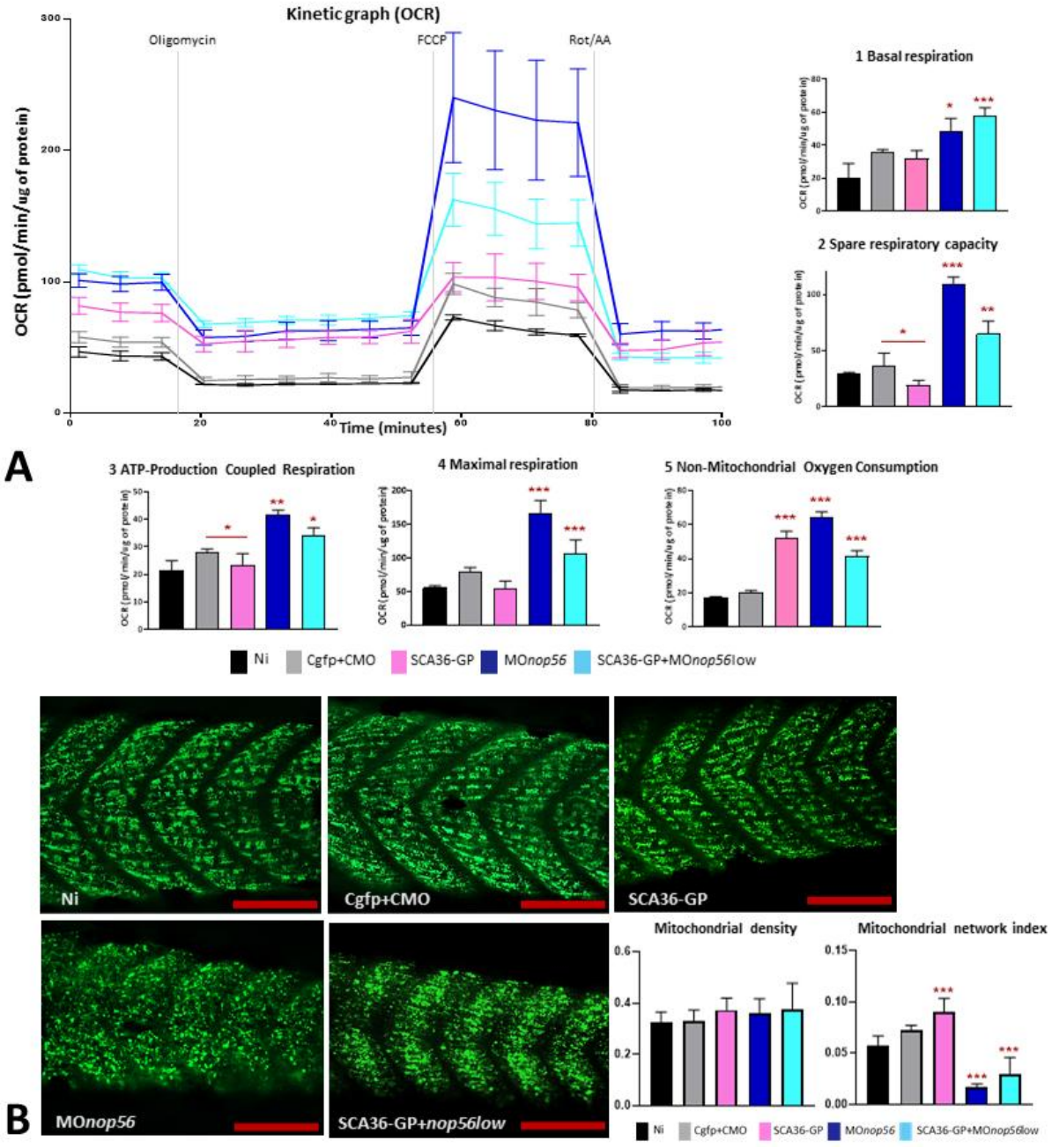
metabolites in SCA36-GP+MO*nop56*low. Upregulated metabolites are shown in red, downregulated metabolites in green and analyzed metabolites but not significant in bold black.

Integrative metabolomics and proteomics analyses identified significant alterations in multiple metabolic pathways in the SCA36-GP+MO*nop56*low group (all pathways showing *p*-values < 0.03 and pathway impact values > 0.28; with all values > 0.45 except for aminoacyl-tRNA biosynthesis) (Fig 7B). The most affected processes included “glycolysis or Gluconeogenesis”, “pyruvate metabolism”, “citrate (TCA) cycle”, and “pentose phosphate pathway”. In addition, several amino acid biosynthetic pathways and “aminoacyl-tRNA biosynthesis”, were significantly affected. Additional changes were observed in “glyoxylate and dicarboxylate metabolism”, “fructose and mannose metabolism”, “one carbon pool by folate” and “riboflavin metabolism”. The “neomycin, kanamycin and gentamicin biosynthesis” pathway, was also enriched driven by increased abundance of intermediates such as glucose and glucose-6-phosphate. A summary of significant altered pathways in SCA36-GP+MO*nop56*low is shown in Fig 7C.

- **Mitochondrial respiration and mitochondrial organization are altered in SCA36-GP, MO*nop56* and SCA36-GP+MO*nop56*low groups**

Proteomic and metabolomic analyses revealed convergent alterations affecting energy metabolism and mitochondrial-related pathways. Proteomic changes suggested disruptions in energy metabolism, ribosome function, amino acid metabolism and proteins associated with mitochondrial respiration in combined and SCA36-GP conditions, while metabolomics indicated profound remodelling of glycolysis, TCA cycle, and amino acid biosynthesis, as well as changes in protein synthesis and nitrogen metabolism in both *nop56* groups but not in SCA36-GP. These results suggested potential mitochondrial dysfunction or compensatory mitochondrial activity, motivating the assessment of mitochondrial respiration using Seahorse analysis.

Seahorse analysis of mitochondrial respiration (Fig 8A) revealed that under basal conditions, mitochondrial respiration was significantly increased in MO*nop56* and SCA36-GP+MO*nop56*low groups. Following the sequential injection of modulators, spare respiratory capacity, maximal respiration, and ATP-linked respiration were also significantly elevated in these two groups. In contrast, SCA36-GP embryos displayed reduced spare respiratory capacity and ATP-linked respiration compared to injected controls, despite the absence of significant changes in basal or maximal respiration. Additionally, non-mitochondrial oxygen consumption was significantly increased not only in MO*nop56* and SCA36-GP+MO*nop56*low groups but also in the SCA36-GP group.



588

589 **Figure 8. A. Seahorse analysis of mitochondrial respiration in zebrafish larvae. Basal respiration, spare respiratory capacity,**
590 **ATP-production coupled respiration, maximal respiration, and non-mitochondrial oxygen consumption were measured in**
591 **Control Ni (non-injected), control GFP, SCA36-GP, MO*nop56*, and SCA36-GP+MO*nop56*low groups. Basal and maximal**
592 **respiration, spare capacity, and ATP-linked respiration are significantly increased in MO*nop56* and SCA36-**
593 **GP+MO*nop56*low larvae. In SCA36-GP, spare respiratory capacity and ATP-production coupled respiration are significantly**
594 **reduced in comparison with Cgfp+CMO. Non-mitochondrial oxygen consumption is elevated in all three experimental**
595 **groups compared with controls. B. *tomm20* mitochondria fluorescence revealed statistically a significant reduction in**
596 **mitochondrial network index in MO*nop56* and SCA36-GP+MO*nop56*low, whereas SCA36-GP embryos showed a significant**

increase compared with controls. No significant differences in mitochondrial density were observed across groups. Data are presented as mean + standard error of the mean (SEM). Significance indicated with * $p < 0.05$, $p < 0.01$ or *** $p < 0.001$.**

To further assess mitochondrial organization, a transgenic *tomm20* reporter line was used to visualize mitochondria (Fig 8B). This analysis revealed a significant reduction in mitochondrial network index in both MO*nop56* and SCA36-GP+MO*nop56*low groups, indicating a more fragmented organization in muscle fibers. In contrast, SCA36-GP embryos displayed a significantly increased mitochondrial network index compared to all other experimental conditions, suggesting enhanced mitochondrial connectivity or network remodelling. Notably, no significant differences were observed in mitochondrial density across conditions, suggesting that these changes reflect alterations in mitochondrial organization rather than mitochondrial abundance.

Discussion

Our findings show that poly-GP expression alone produces detectable cellular and functional alterations *in vivo*, including locomotor impairment, p62-positive aggregates and increased apoptosis. Importantly, our proteomic analysis suggests that poly-GP expression affects pathways involved in protein homeostasis, with alterations in ribosome and proteasome related proteins. We observed widespread changes in the abundance of ribosomal proteins, suggesting that poly-GP expression not only involves formation of protein aggregates, but may also affect protein synthesis. This is consistent with previous results suggesting that poly-GP may directly interfere with translational processes. The elongation phase of translation has been reported to be slower in the GP frame than in other C9ORF72 DPR frames, with the proline-rich nature of poly-GP proposed as a potential contributor to slower ribosome progression (33). Consistent with this, poly-GP repeats have been identified as sequences capable of inducing ribosome stalling and activating ribosome-associated quality control pathways (34). These results are particularly relevant in SCA36, as previous studies have pointed to ribosomal

dysfunctions, impaired translation and alternative splicing as potential molecular alterations in SCA36 pathogenesis, consistent with the NOP56 role in ribosome biogenesis (5,6,35). Together, these data suggest that poly-GP may contribute to SCA36 pathogenesis by perturbing both protein synthesis and degradation.

Interestingly, recent studies in *Drosophila* proposed that SCA36 neurodegeneration arises through combinatorial interactions between repeat-associated RNA toxicity and DPR accumulation, identifying poly-GP as the most toxic DPR in that model (21). In line with these findings, we investigated whether altered NOP56 function could modify the effects of poly-GP accumulation. Our results show that partial reduction of *nop56* markedly modifies the response to poly-GP accumulation, causing neuropathological phenotypes and inducing widespread metabolic remodelling. These results support a model in which NOP56 acts as a critical modulator of poly-GP toxicity, and alterations in its function influence cellular vulnerability to DPR accumulation. Locomotor defects were observed in the three experimental conditions, while MO*nop56* and SCA36-GP+MO*nop56*low groups additionally showed motor neuron defects, cerebellar malformation and myosin-associated muscular abnormalities These phenotypes affect the same structures compromised in SCA36 patients, in whom cerebellar atrophy, locomotor deficits and motor neuron dysfunction are cardinal features (1,2,36,37). The cerebellar alterations we observe arise during development and therefore reflect regional vulnerability to poly-GP and reduced nop56 levels rather than the progressive atrophy characteristic of the adult disease. In concordance with our data, p62 aggregation has been reported in the inferior olivary nucleus of SCA36 patients, but not in the cerebellum or cortex (7,20). Interestingly, myosin-related abnormalities have not been previously described in SCA36, potentially providing new insights into the systemic manifestations of the disease and requiring further investigation in patient tissues.

To further validate the effects observed following *nop56* downregulation, we analysed *nop56* heterozygous mutants. Similar to the morpholino injected embryos, *nop56* heterozygous mutants displayed poly-GP accumulation, locomotor impairment, and motor neuron abnormalities, without

gross morphological defects, suggesting that even partial reduction of *nop56* function is sufficient to enhance poly-GP accumulation and exacerbate its associated neurotoxicity. The milder phenotype observed in *nop56* heterozygotes compared to morpholino injected embryos most likely reflects maternal contribution effects, where heterozygotes retain one functional allele and maternal contribution may additionally compensate for early loss of nop56 function in the mutants, as previously proposed in zebrafish models (38), whereas the morpholino blocks translation of both zygotic and maternally deposited transcripts. These findings further support the idea that even modest reductions in *nop56* levels are sufficient to modify the response to poly-GP accumulation. Whether these early alterations progress to age-dependent neurodegeneration remains an open question that will require stable adult zebrafish models.

Interestingly, similar interactions between loss-of-function and poly-GP mediated toxicity have also recently been described in C9ORF72-associated ALS/FTD (22). In this case, these interactions result in autophagy defects, p62 aggregation, locomotor impairment and motor neuron apoptosis. Ribosome and mitochondria dysfunction were also described as major pathways affected in this model (22). In our models, poly-GP expression also resulted in p62-positive inclusions, not only in the combined condition but also in SCA36-GP embryos, indicating accumulation of autophagy substrates. Interestingly, p62 accumulation was more prominent in SCA36-GP than in the combined model, suggesting that p62 accumulation may not directly correlate with disease severity, but instead reflect degradation capacity and cell survival. In addition, TUNEL staining revealed increased apoptosis in all three experimental conditions, with a broader and more pronounced distribution in the combined model, suggesting increased cellular vulnerability under conditions of poly-GP expression and reduced *nop56* function. Although the identity of these apoptotic cells remains to be determined, their distribution in nervous system and muscle-associated regions suggests that both developmental defects and early neurodegenerative processes may contribute to the observed phenotypes.

Comparative proteomic analysis of poly-GP-GFP immunoprecipitates, using GFP alone as control, revealed proteins differentially associated with poly-GP in SCA36-GP and SCA36-GP+MO*nop56*low models, particularly affecting ribosome function, RNA splicing, protein degradation, metabolism and cellular stress responses, with stronger differences in the combined model. To our knowledge, this represents the first characterization of the SCA36 poly-GP interactome *in vivo*. RNA-binding and spliceosomal proteins were less represented in poly-GP precipitates than in GFP controls, particularly in SCA36-GP+MO*nop56*low, while GSEA showed reduced representation of rRNA processing, translation and nonsense-mediated decay pathways in both models. These findings suggest that poly-GP expression is associated with broad perturbation of RNA metabolism and translational processes, further accentuated by partial *nop56* depletion. In addition, proteasomal, lysosomal and autophagy-related processes were consistently enriched in both models, particularly in SCA36-GP+MO*nop56*low. Importantly, the coordinated enrichment detected by GSEA indicates that these changes are not restricted to a few individual proteins but affect entire functional modules of the poly-GP interactome, particularly those related to proteostasis and RNA metabolism. The association of poly-GP with the degradation machinery suggests that it is actively targeted for clearance and its increased accumulation upon *nop56* depletion may reflect limiting clearance capacity, rather than increased production. Proteins involved in metabolism and mitochondrial function, were also differentially associated with poly-GP, particularly in the combined model, together with pathways linked with DNA damage, apoptosis, and immune responses. Reactome-based GSEA revealed enrichment of immune system pathways particularly in SCA36-GP, together with apoptotic and DNA damage response pathways in both models. The combined model additionally showed reduced representation of cell-cycle, signal transduction pathways, motor proteins and proteins relevant for CNS processes, including Smndc1, which has been linked to motor neuron survival. Together, these findings indicate that poly-GP engages a broad range of cellular processes, which is further modified by partial *nop56* depletion.

Moreover, several ALS-associated proteins were less represented in poly-GP precipitates than in GFP controls, including Fus and Sod1 in both conditions, and Taf15 only in the combined model. Fus and

Taf15 share extensive RNA interaction profiles and associate with spliceosomal complexes (39), consistent with the reduced representation of spliceosomal components described above. STRING network analysis indicated that these proteins cluster with ribosomal proteins (including NOP56) forming a tight connected network, suggesting that the observed changes affect a coordinated group of interacting partners. Previous studies revealed that poly-PR and poly-GR derived from the C9ORF72 expansion interact with NOP56, altering the nucleolar localization of NOP56 and fibrillarin (40). NOP56 has also been implicated in SOD1-associated ALS, where its dysregulation contributes to motor neuron degeneration and astroglial dysfunction (41,42). Consistent with this, *nop56* loss-of-function reduces the expression of zebrafish orthologs of several ALS-related genes, including *c9orf72*, *fus*, and *tardbp* (8). Most recently, heterozygous *Nop56* mice were shown to develop ubiquitin positive inclusions containing cytoplasmic TDP-43, a hallmark of ALS pathology (9). These results support molecular connections between SCA36 and ALS involving RNA processing, ribosome biology and protein homeostasis and suggest that poly-GP alters the association of ALS-related RNA-binding proteins with the translational machinery.

The metabolic and mitochondrial alterations identified at the proteomic level were further supported and extended by metabolomic profiling. Partial *nop56* knockdown profoundly altered the metabolic response to poly-GP expression. To our knowledge, this represents the first metabolomic characterization of zebrafish models of SCA36 and poly-GP toxicity. The SCA36-GP+MO*nop56*low embryos showed profound metabolic remodelling, including major alterations in glycolysis, pyruvate metabolism, TCA cycle, and pentose phosphate pathway, consistent with extensive mitochondrial remodelling, mitochondrial stress, and altered redox homeostasis. Several metabolites involved in oxidative stress responses were altered, including elevated proline and arginine (43,44). These changes were accompanied by increases in cysteine, inosine and riboflavin, metabolites implicated in antioxidant responses, together with a reduction in oxidized glutathione (GSSG), which may indicate protection from oxidative stress (45,46). In contrast, methionine and uric acid, both implicated in neuroprotection against oxidative stress, were significantly reduced (45,47). The direction of these

723 changes is therefore not uniform, with some metabolites consistent with an enhanced antioxidant
724 response and others with reduced protective capacity. Rather than a single oxidative signature, this
725 mixed profile suggests a complex metabolic adaptation to redox imbalance.

726 Branched-chain amino acids (valine, leucine, isoleucine) were among the most strongly upregulated
727 metabolites in the combined group. While normally important for energy metabolism, their
728 accumulation has been associated with neurotoxicity, oxidative stress and inflammation via mTOR
729 activation and mitochondria dysfunction (48). In line with these alterations, NADPH was elevated in
730 SCA36-GP+MO*nop56*low embryos, consistent with an enhanced redox imbalance. Creatine levels were
731 also significantly reduced, consistent with muscle dysfunction and in agreement with findings in ALS
732 models, where decreased creatine correlates with reduced survival and creatine supplementation
733 confers neuroprotection (49).

734 Metabolic alterations also affected energy production and neurotransmitter metabolism. Alterations
735 in the TCA cycle may be partially compensated by glutaminolysis, an alternative pathway that
736 maintains ATP production under mitochondrial stress through increasing glutamine catabolism to form
737 TCA intermediates (50). However, glutamate, a neurotransmitter derived from glutamine, was
738 decreased, together with precursors such as glycine, phenylalanine, tyrosine, l-alanine and
739 phosphocholine. These results indicate a potential impairment in neurotransmitter metabolism and
740 biosynthetic pathways. Elevated N-acetylaspartate may further reflect alterations in neurotransmitter
741 metabolism and neuronal vulnerability, as previously described in Canavan disease (51). Although
742 MO*nop56* and SCA36-GP+MO*nop56*low conditions shared most altered metabolic pathways, the
743 combined model exhibited additional changes affecting neurotransmitter metabolism, with glycine,
744 phenylalanine, tyrosine, L-alanine and N-acetylaspartate remaining unaltered in MO*nop56*. These
745 findings suggest that poly-GP expression does not result in a completely distinct metabolic profile, but
746 rather further modifies the metabolic alterations derived from reduced *nop56* function, particularly
747 regarding neurotransmitter metabolism.

748 Reduced levels of diverse acylcarnitines suggest impaired fatty acid oxidation, which has also been
749 reported in ALS (52). However, elevated glucose levels in the combined model may represent a
750 compensatory response to sustain high demand of energy production, as observed in ALS and other
751 neurodegenerative diseases (53,54). Notably, acylcarnitine supplementation has been reported to
752 exert neuroprotective effects by enhancing mitochondrial function, antioxidant activity and cholinergic
753 neurotransmission (55,56). Similar to our data, previous metabolic analysis in other ALS models
754 revealed impaired glycolysis, TCA cycle, fatty acid metabolism and neurotransmitter levels (57–59).

755 Notably, the SCA36-GP model displayed only minimal metabolic alterations despite clear proteomic
756 changes and locomotor impairment, suggesting that early proteostatic and cytoskeletal alterations are
757 sufficient to compromise motor performance before metabolic alterations occur. In contrast, the
758 broader metabolic remodelling observed in the SCA36-GP+MO*nop56*low condition, suggests that
759 partial *nop56* deficiency is sufficient to promote lower cellular resilience that may contribute to
760 oxidative stress and neurodegeneration. These findings support the idea that partial *nop56* loss acts
761 as a critical modifier of poly-GP toxicity by lowering the threshold for metabolic dysfunction.

762 Seahorse assays revealed increased mitochondrial respiratory activity in MO*nop56* and SCA36-
763 GP+MO*nop56l*ow models, potentially reflecting an early compensatory response or, alternatively,
764 maladaptive mitochondrial overactivation aimed at maintaining ATP production under cellular stress.
765 TOMM20 analysis also revealed disorganization of mitochondrial distribution patterns within muscle
766 fibers without changes in mitochondria density in both models. Given the close spatial relationship
767 between mitochondria and muscle fiber architecture, these alterations may partially reflect underlying
768 cytoskeletal and muscle disorganization. In contrast, SCA36-GP embryos displayed increased
769 mitochondrial network connectivity together with reduced ATP-linked respiration and spare
770 respiratory capacity, suggesting an early adaptive mitochondrial response. While reduced
771 mitochondrial respiration is commonly reported in ALS, Alzheimer's disease, Parkinson's disease, and
772 Friedreich's ataxia (60,61) hyperactivation has also been described in fragile X-associated

tremor/ataxia syndrome (62,63). Importantly, elevated non-mitochondrial oxygen consumption across all groups, including SCA36-GP, may reflect increased ROS production and oxidative stress, consistent with our proteomic and metabolomic findings.

Several limitations of this study should be acknowledged. Our analyses were performed during embryonic and early larval stages of a late-onset disorder, so the alterations described here represent early events rather than established neurodegeneration. Poly-GP was expressed from an injected plasmid, resulting in mosaic expression at levels that do not necessarily reflect those reached in patients. Proteomic and metabolomic profiling was performed on whole embryos, so the tissue origin of the observed changes cannot be resolved. Finally, *nop56* was depleted using a morpholino, an approach associated with potential off-target effects. The reproduction of the main phenotypes in *nop56* heterozygous mutants supports the specificity of these findings.

Taken together, our findings indicate that poly-GP toxicity is markedly exacerbated by partial loss of *nop56* function, causing metabolic and phenotypic alterations that converge on pathways shared with ALS and other neurodegenerative diseases. Ribosome dysfunction, RNA splicing defects, altered mitochondrial organization and respiratory activity, redox imbalance, and impaired neurotransmitter metabolism emerge as central molecular alterations in this context. Importantly, these molecular changes are accompanied by pronounced physiological defects, including motor neuron abnormalities, cerebellar malformation, impaired locomotion, p62-positive aggregates and TUNEL positive apoptosis, affecting the structures compromised in SCA36 patients. Notably, myosin-associated muscular dysfunction and mitochondrial alterations have not been previously reported in SCA36 patients, providing novel insights into the systemic manifestations of the disease. By integrating proteomic, metabolomic and functional analyses, we provide the first systems-level characterization of poly-GP toxicity in the context of reduced *nop56* function. Our model isolates the contribution of the poly-GP DPR from the remaining DPRs and from repeat-derived RNA toxicity, which has been proposed to act combinatorially with DPR accumulation in SCA36 (21). How these two mechanisms interact in patient-

derived systems remains to be established. Future studies will determine whether the early alterations described here evolve into progressive neurodegeneration in stable adult models and their potential modulation by therapeutic interventions.

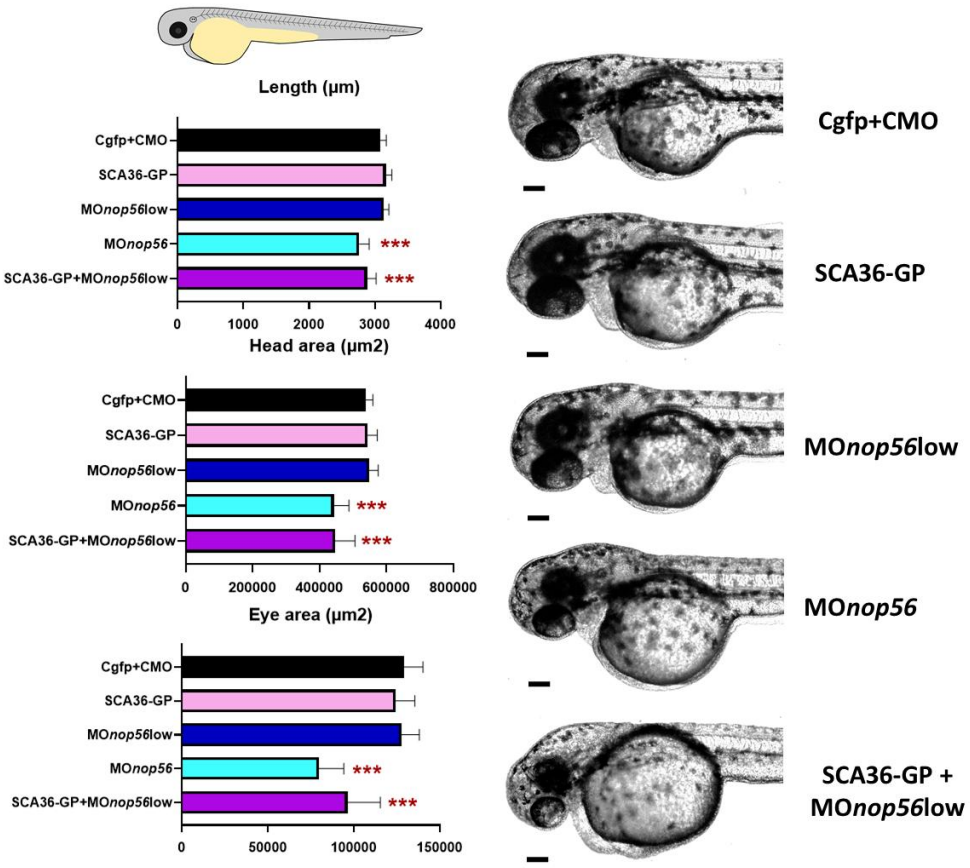
Conclusions

In conclusion, our study identifies partial *nop56* deficiency as a critical modifier of poly-GP toxicity, amplifying its molecular, functional and metabolic consequences. Integrated proteomic, metabolomic and functional analyses revealed that poly-GP associates with ribosomal and RNA-binding proteins and with the degradation machinery and its accumulation is accompanied mitochondrial alterations and metabolic remodelling, linking SCA36 with convergent mechanisms previously described in ALS and related neurodegenerative disorders. These findings delineate pathways that may inform future biomarker and therapeutic studies in SCA36.

Supplemental data

Supplementary table 1: Complete proteomic dataset with ANOVA statistical analysis.

Supplementary table 2: Results of the metabolomic analysis with Student's t-test statistics.

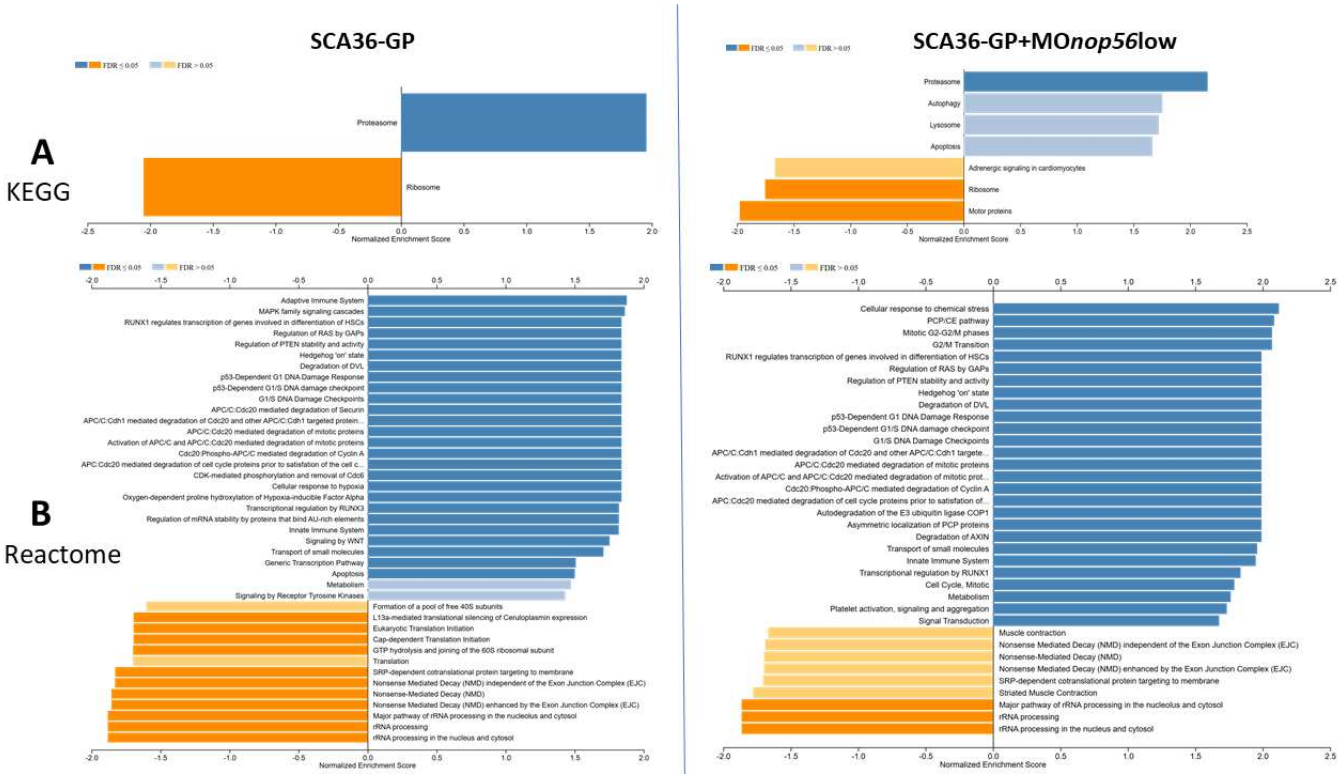


814

815 **Supplemental figure 1. Phenotypic characterization of all the conditions. Data in the graphs presented as mean +**

816 **standard error of the mean (SEM). Significance indicated with* p < 0.05**, p < 0.01 or *** p < 0.001. Scale bars: 100µm.**

817



Supplemental figure 2. GSEA analysis based in FDR<0.1 revealed A. KEGG significant altered pathways and B Reactome significant altered pathways in SCA36-GP and SCA36-GP+MO*nop56*low groups in comparison with control.

List of abbreviations

ACN: Acetonitrile.

ALS: Amyotrophic lateral sclerosis.

ASO: antisense oligonucleotide.

C9 ALS/FTD: C9ORF72 associated Amyotrophic lateral sclerosis or frontotemporal dementia.

CNS: Central nervous system.

dpf: days post fertilization.

DPR: Dipeptide repeat protein.

EZRC: European Zebrafish Resource Center.

FCCP: Fluorocarbonyl cyanide phenylhydrazone.

FDR: False discovery rate.

FTD: Frontotemporal dementia.

GFP: Green fluorescent protein.

GSSG: Oxidized glutathione.

GSEA: Gene set enrichment analysis.

hpf: hours post fertilization.

KEGG: Kyoto Encyclopedia of Genes and Genomes.

LC-MS: Liquid chromatography–mass spectrometry.

MO: Morpholino oligonucleotide.

MS: Mass spectrometry.

Ni: Non injected control embryos.

PCA: Principal component analysis.

PLS-DA: Partial least squares discriminant analysis.

Poly-GP: Glycine-proline dipeptide repeat protein.

RAN: Repeat-associated non-ATG.

ROS: Reactive oxygen species.

RT: room temperature.

SCA36: Spinocerebellar ataxia type 36.

TEER: Touched-Evoked Escape Response.

TUNEL: Terminal deoxynucleotidyl transferase dUTP nick end labelling.

VIP: Variable importance in projection.

WT: Wild type.

Ethics approval and consent to participate

Zebrafish experimental procedures were approved by the National and Institutional Ethical Committees (code: 26775).

Consent for publication

Not applicable.

Availability of data and materials

All data generated or analyzed during this study are included in this article and its supplementary information files.

Competing interests

The authors declare no competing interests.

Funding

This work has been supported by FRC (Fédération pour la Recherche sur le Cerveau) project: Translation of repeat expansion mutations into toxic proteins as a common pathogenic mechanism in microsatellite neurodegenerative diseases. AQR was supported by a postdoctoral fellowship from the Xunta de Galicia.

Author contributions

A. Q.-R.: Conceptualization; Investigation; Methodology; Data curation; Formal analysis; Writing—original draft. M. B.: Proteomic methodology and investigation. A.L.: Development of mitochondrial image analysis and quantification methods; review and editing. M.F.: Writing—review and editing. I.N.: Metabolomic and Seahorse methodology. N. C.-B.: Conceptualization; Investigation; Methodology;

Writing—review and editing. E. K.: Conceptualization; Supervision; Funding acquisition; Project administration; Writing—review and editing.

Acknowledgements

We thank Prof. Richard Hawkes for kindly providing the zebrin II antibody and Dr. Antón Villa-Sanjurjo for scientific advice.

References

1. Kobayashi H, Abe K, Matsuura T, Ikeda Y, Hitomi T, Akechi Y, et al. Expansion of Intronic GGCCTG Hexanucleotide Repeat in NOP56 Causes SCA36, a Type of Spinocerebellar Ataxia Accompanied by Motor Neuron Involvement. The American Journal of Human Genetics. 2011 Jul;89(1):121–30. doi:10.1016/j.ajhg.2011.05.015

2. García-Murias M, Quintáns B, Arias M, Seixas AI, Cacheiro P, Tarrío R, et al. 'Costa da Morte' ataxia is spinocerebellar ataxia 36: clinical and genetic characterization. Brain. 2012 May;135(5):1423–35. doi:10.1093/brain/aws069

3. DeJesus-Hernandez M, Mackenzie IR, Boeve BF, Boxer AL, Baker M, Rutherford NJ, et al. Expanded GGGGCC Hexanucleotide Repeat in Noncoding Region of C9ORF72 Causes Chromosome 9p-Linked FTD and ALS. Neuron. 2011 Oct;72(2):245–56. doi:10.1016/j.neuron.2011.09.011

4. Renton AE, Majounie E, Waite A, Simón-Sánchez J, Rollinson S, Gibbs JR, et al. A Hexanucleotide Repeat Expansion in C9ORF72 Is the Cause of Chromosome 9p21-Linked ALS-FTD. Neuron. 2011 Oct;72(2):257–68. doi:10.1016/j.neuron.2011.09.010

5. Matsuzono K, Imamura K, Murakami N, Tsukita K, Yamamoto T, Izumi Y, et al. Antisense Oligonucleotides Reduce RNA Foci in Spinocerebellar Ataxia 36 Patient iPSCs. Molecular Therapy - Nucleic Acids. 2017 Sep;8:211–9. doi:10.1016/j.omtn.2017.06.017

6. Morikawa T, Miura S, Uchiyama Y, Hiruki S, Sun Y, Fujioka R, et al. Hexanucleotide repeat expansion in SCA36 reduces the expression of genes involved in ribosome biosynthesis and protein translation. J Hum Genet. 2024 Sep;69(9):411–6. doi:10.1038/s10038-024-01260-7

7. McEachin ZT, Gendron TF, Raj N, García-Murias M, Banerjee A, Purcell RH, et al. Chimeric Peptide Species Contribute to Divergent Dipeptide Repeat Pathology in c9ALS/FTD and SCA36. Neuron. 2020 Jul;107(2):292-305.e6. doi:10.1016/j.neuron.2020.04.011

8. Quelle-Regaldie A, Folgueira M, Yáñez J, Sobrido-Cameán D, Alba-González A, Barreiro-Iglesias A, et al. A nop56 Zebrafish Loss-of-Function Model Exhibits a Severe Neurodegenerative Phenotype. Biomedicines. 2022 Jul 28;10(8):1814. doi:10.3390/biomedicines10081814

9. Matsuzono K, Nagao Y, Sarai C, Takayanagi Y, Sakashita E, Sekiguchi K, et al. NOP56 is essential for mammalian generation and maintenance of multiple central nervous systems, associated with SCA36 pathology. acta neuropathol commun. 2026 Jul 12. doi:10.1186/s40478-026-02379-8

10. Almeida S, Gascon E, Tran H, Chou HJ, Gendron TF, DeGroot S, et al. Modeling key pathological features of frontotemporal dementia with C9ORF72 repeat expansion in iPSC-derived human neurons. Acta Neuropathol. 2013 Sep;126(3):385–99. doi:10.1007/s00401-013-1149-y

11. Ash PEA, Bieniek KF, Gendron TF, Caulfield T, Lin WL, DeJesus-Hernandez M, et al. Unconventional Translation of C9ORF72 GGGGCC Expansion Generates Insoluble Polypeptides Specific to c9FTD/ALS. Neuron. 2013 Feb;77(4):639–46. doi:10.1016/j.neuron.2013.02.004

12. Mori K, Arzberger T, Grässer FA, Gijselinck I, May S, Rentzsch K, et al. Bidirectional transcripts of the expanded C9orf72 hexanucleotide repeat are translated into aggregating dipeptide repeat proteins. Acta Neuropathol. 2013 Dec;126(6):881–93. doi:10.1007/s00401-013-1189-3

13. Zu T, Liu Y, Bañez-Coronel M, Reid T, Pletnikova O, Lewis J, et al. RAN proteins and RNA foci from antisense transcripts in *C9ORF72* ALS and frontotemporal dementia. Proc Natl Acad Sci USA. 2013 Dec 17;110(51). doi:10.1073/pnas.1315438110

14. Todd TW, McEachin ZT, Chew J, Burch AR, Jansen-West K, Tong J, et al. Hexanucleotide Repeat Expansions in c9FTD/ALS and SCA36 Confer Selective Patterns of Neurodegeneration In Vivo. Cell Reports. 2020 May;31(5):107616. doi:10.1016/j.celrep.2020.107616

15. Hasumi M, Ito H, Machida K, Niwa T, Taminato T, Nagai Y, et al. Dissecting the mechanism of NOP56 GGCCUG repeat-associated non-AUG translation using cell-free translation systems. Journal of Biological Chemistry. 2025 Apr;301(4):108360. doi:10.1016/j.jbc.2025.108360

16. Wilson KM, Katona E, Glaria I, Carcolé M, Swift IJ, Sogorb-Esteve A, et al. Development of a sensitive trial-ready poly(GP) CSF biomarker assay for *C9orf72* -associated frontotemporal dementia and amyotrophic lateral sclerosis. J Neurol Neurosurg Psychiatry. 2022 Jul;93(7):761–71. doi:10.1136/jnnp-2021-328710

17. McEachin ZT, Chung M, Stratton SA, Han C, Kim WJ, Sheth U, et al. Molecular impact of antisense oligonucleotide therapy in C9orf72-associated ALS. Cell. 2025 Aug;S0092867425009080. doi:10.1016/j.cell.2025.07.045

18. Mackenzie IRA, Frick P, Grässer FA, Gendron TF, Petrucelli L, Cashman NR, et al. Quantitative analysis and clinico-pathological correlations of different dipeptide repeat protein pathologies in C9ORF72 mutation carriers. Acta Neuropathol. 2015 Dec;130(6):845–61. doi:10.1007/s00401-015-1476-2

19. Saberi S, Stauffer JE, Schulte DJ, Ravits J. Neuropathology of Amyotrophic Lateral Sclerosis and Its Variants. Neurologic Clinics. 2015 Nov;33(4):855–76. doi:10.1016/j.ncl.2015.07.012

20. Liu W, Ikeda Y, Hishikawa N, Yamashita T, Deguchi K, Abe K. Characteristic RNA foci of the abnormal hexanucleotide GGCCUG repeat expansion in spinocerebellar ataxia type 36 (A sidan). Euro J of Neurology. 2014 Nov;21(11):1377–86. doi:10.1111/ene.12491

21. Hsiao CT, Fu SJ, Guo TN, Lin CC, Tsao YJ, Chang W, et al. A fly model of SCA36 reveals combinatorial neurotoxicity of hexanucleotide and dipeptide repeats. Wang H, editor. PLoS Genet. 2025 Dec 3;21(12):e1011954. doi:10.1371/journal.pgen.1011954

22. De Calbiac H, Renault S, Haouy G, Jung V, Roger K, Zhou Q, et al. Poly-GP accumulation due to C9orf72 loss of function induces motor neuron apoptosis through autophagy and mitophagy defects. Autophagy. 2024 Oct 2;20(10):2164–85. doi:10.1080/15548627.2024.2358736

23. Arribat Y, Grepper D, Lagarrigue S, Richard J, Gachet M, Gut P, et al. Mitochondria in Embryogenesis: An Organellogenesis Perspective. Front Cell Dev Biol. 2019 Nov 22;7:282. doi:10.3389/fcell.2019.00282

24. Schindelin J, Arganda-Carreras I, Frise E, Kaynig V, Longair M, Pietzsch T, et al. Fiji: an open-source platform for biological-image analysis. Nat Methods. 2012 Jul;9(7):676–82. doi:10.1038/nmeth.2019

25. Boudaoud A, Burian A, Borowska-Wykręt D, Uyttewaal M, Wrzalik R, Kwiatkowska D, et al. FibrilTool, an ImageJ plug-in to quantify fibrillar structures in raw microscopy images. Nat Protoc. 2014 Feb;9(2):457–63. doi:10.1038/nprot.2014.024

26. Santos D, Monteiro SM, Luzio A. General Whole-Mount Immunohistochemistry of Zebrafish (Danio rerio) Embryos and Larvae Protocol. In: Félix L, editor. Teratogenicity Testing [Internet]. New York, NY: Springer New York; 2018 [cited 2025 Oct 10]. p. 365–71. (Methods in Molecular Biology). Available from: http://link.springer.com/10.1007/978-1-4939-7883-0_19 doi:10.1007/978-1-4939-7883-0_19

27. Walker JM. The Bicinchoninic Acid (BCA) Assay for Protein Quantitation. In: Walker JM, editor. The Protein Protocols Handbook [Internet]. Totowa, NJ: Humana Press; 2009 [cited 2025 Oct 10]. p. 11–5. (Springer Protocols Handbooks). Available from: http://link.springer.com/10.1007/978-1-59745-198-7_3 doi:10.1007/978-1-59745-198-7_3

28. Swift ML. GraphPad Prism, Data Analysis, and Scientific Graphing. J Chem Inf Comput Sci. 1997 Mar 1;37(2):411–2. doi:10.1021/ci960402j

29. Hulsen T, De Vlieg J, Alkema W. BioVenn – a web application for the comparison and visualization of biological lists using area-proportional Venn diagrams. BMC Genomics. 2008;9(1):488. doi:10.1186/1471-2164-9-488

30. Ge SX, Jung D, Yao R. ShinyGO: a graphical gene-set enrichment tool for animals and plants. Valencia A, editor. Bioinformatics. 2020 Apr 15;36(8):2628–9. doi:10.1093/bioinformatics/btz931

31. Mering CV. STRING: a database of predicted functional associations between proteins. Nucleic Acids Research. 2003 Jan 1;31(1):258–61. doi:10.1093/nar/gkg034

32. Pang Z, Lu Y, Zhou G, Hui F, Xu L, Viau C, et al. MetaboAnalyst 6.0: towards a unified platform for metabolomics data processing, analysis and interpretation. Nucleic Acids Research. 2024 Jul 5;52(W1):W398–406. doi:10.1093/nar/gkae253

33. Latallo MJ, Wang S, Dong D, Nelson B, Livingston NM, Wu R, et al. Single-molecule imaging reveals distinct elongation and frameshifting dynamics between frames of expanded RNA repeats in C9ORF72-ALS/FTD. Nat Commun. 2023 Sep 11;14(1):5581. doi:10.1038/s41467-023-41339-x

34. Chen KY, Park H, Subramaniam AR. Massively parallel identification of sequence motifs triggering ribosome-associated mRNA quality control. Nucleic Acids Research. 2024 Jul 8;52(12):7171–87. doi:10.1093/nar/gkae285

35. Lykke-Andersen S, Ardal BK, Hollensen AK, Damgaard CK, Jensen TH. Box C/D snoRNP Autoregulation by a cis-Acting snoRNA in the NOP56 Pre-mRNA. Molecular Cell. 2018 Oct;72(1):99-111.e5. doi:10.1016/j.molcel.2018.08.017

36. Ikeda Y, Ohta Y, Kobayashi H, Okamoto M, Takamatsu K, Ota T, et al. Clinical features of SCA36: A novel spinocerebellar ataxia with motor neuron involvement (Asidan). Neurology. 2012 Jul 24;79(4):333–41. doi:10.1212/WNL.0b013e318260436f

37. Arias M, García-Murias M, Sobrido MJ. Spinocerebellar ataxia 36 (SCA36): "Costa da Morte ataxia". Neurología (English Edition). 2017 Jul;32(6):386–93. doi:10.1016/j.nrleng.2014.11.004

38. Abrams EW, Mullins MC. Early zebrafish development: It's in the maternal genes. Current Opinion in Genetics & Development. 2009 Aug;19(4):396–403. doi:10.1016/j.gde.2009.06.002

39. Kapeli K, Pratt GA, Vu AQ, Hutt KR, Martinez FJ, Sundararaman B, et al. Distinct and shared functions of ALS-associated proteins TDP-43, FUS and TAF15 revealed by multisystem analyses. Nat Commun. 2016 Jul 5;7(1):12143. doi:10.1038/ncomms12143

40. Hartmann H, Hornburg D, Czuppa M, Bader J, Michaelsen M, Farny D, et al. Proteomics and *C9orf72* neuropathology identify ribosomes as poly-GR/PR interactors driving toxicity. Life Sci Alliance. 2018 May;1(2):e201800070. doi:10.26508/lsa.201800070

41. Miyazaki K, Yamashita T, Morimoto N, Sato K, Mimoto T, Kurata T, et al. Early and selective reduction of NOP56 (Asidan) and RNA processing proteins in the motor neuron of ALS model mice. Neurological Research. 2013 Sep;35(7):744–54. doi:10.1179/1743132813Y.0000000196

42. Miller SJ, Zhang P wu, Glatzer J, Rothstein JD. Astroglial transcriptome dysregulation in early disease of an ALS mutant SOD1 mouse model. Journal of Neurogenetics. 2017 Apr 3;31(1–2):37–48. doi:10.1080/01677063.2016.1260128

43. Ben Rejeb K, Abdelly C, Savouré A. How reactive oxygen species and proline face stress together. Plant Physiology and Biochemistry. 2014 Jul;80:278–84. doi:10.1016/j.plaphy.2014.04.007

44. Liang M, Wang Z, Li H, Cai L, Pan J, He H, et al. l-Arginine induces antioxidant response to prevent oxidative stress via stimulation of glutathione synthesis and activation of Nrf2 pathway. Food and Chemical Toxicology. 2018 May;115:315–28. doi:10.1016/j.fct.2018.03.029

45. Bin P, Huang R, Zhou X. Oxidation Resistance of the Sulfur Amino Acids: Methionine and Cysteine. BioMed Research International. 2017;2017:1–6. doi:10.1155/2017/9584932

46. Basile MS, Bramanti P, Mazzon E. Inosine in Neurodegenerative Diseases: From the Bench to the Bedside. Molecules. 2022 Jul 21;27(14):4644. doi:10.3390/molecules27144644

47. Keizman D, Ish-Shalom M, Berliner S, Maimon N, Vered Y, Artamonov I, et al. Low uric acid levels in serum of patients with ALS: Further evidence for oxidative stress? Journal of the Neurological Sciences. 2009 Oct;285(1–2):95–9. doi:10.1016/j.jns.2009.06.002

48. Zhenyukh O, Civantos E, Ruiz-Ortega M, Sánchez MS, Vázquez C, Peiró C, et al. High concentration of branched-chain amino acids promotes oxidative stress, inflammation and migration of human peripheral blood mononuclear cells via mTORC1 activation. Free Radical Biology and Medicine. 2017 Mar;104:165–77. doi:10.1016/j.freeradbiomed.2017.01.009

49. Guo Q, Hu W, Xu L, Luo H, Wang N, Zhang Q. Decreased serum creatinine levels predict short survival in amyotrophic lateral sclerosis. Ann Clin Transl Neurol. 2021 Feb;8(2):448–55. doi:10.1002/acn3.51299

50. Yang L, Venneti S, Nagrath D. Glutaminolysis: A Hallmark of Cancer Metabolism. Annu Rev Biomed Eng. 2017 Jun 21;19(1):163–94. doi:10.1146/annurev-bioeng-071516-044546

51. Moffett JR, Ross B, Arun P, Madhavarao CN, Namboodiri AMA. N-Acetylaspartate in the CNS: From neurodiagnostics to neurobiology. Progress in Neurobiology. 2007 Feb;81(2):89–131. doi:10.1016/j.pneurobio.2006.12.003

52. Guo K, Savelieff MG, Jang D, Teener SJ, Zhao L, Hur J, et al. Longitudinal Metabolomics in Amyotrophic Lateral Sclerosis Implicates Impaired Lipid Metabolism. Annals of Neurology. 2025 Jul;98(1):19–34. doi:10.1002/ana.27208

53. Ferri A, Coccurello R. What is "Hyper" in the ALS Hypermetabolism? Mediators of Inflammation. 2017;2017:1–11. doi:10.1155/2017/7821672

54. Zanovello M, Sorarù G, Campi C, Anglani M, Spimpolo A, Berti S, et al. Brainstem glucose hypermetabolism in ALS/FTD and shorten survival: a^{18} F-FDG PET/MR study. J Nucl Med. 2021 Sep 9;jnumed.121.262232. doi:10.2967/jnumed.121.262232

55. Jones LL, McDonald DA, Borum PR. Acylcarnitines: Role in brain. Progress in Lipid Research. 2010 Jan;49(1):61–75. doi:10.1016/j.plipres.2009.08.004

56. McCann MR, George De La Rosa MV, Rosania GR, Stringer KA. L-Carnitine and Acylcarnitines: Mitochondrial Biomarkers for Precision Medicine. Metabolites. 2021 Jan 14;11(1):51. doi:10.3390/metabo11010051

57. Dupuis L, Pradat PF, Ludolph AC, Loeffler JP. Energy metabolism in amyotrophic lateral sclerosis. The Lancet Neurology. 2011 Jan;10(1):75–82. doi:10.1016/S1474-4422(10)70224-6

58. Blasco H, Corcia P, Pradat PF, Bocca C, Gordon PH, Veyrat-Durebex C, et al. Metabolomics in Cerebrospinal Fluid of Patients with Amyotrophic Lateral Sclerosis: An Untargeted Approach via High-Resolution Mass Spectrometry. J Proteome Res. 2013 Aug 2;12(8):3746–54. doi:10.1021/pr400376e

59. Loganathan S, Wilson BA, Carey SB, Manzo E, Joardar A, Ugur B, et al. TDP-43 Proteinopathy Causes Broad Metabolic Alterations including TCA Cycle Intermediates and Dopamine Levels in Drosophila Models of ALS. Metabolites. 2022 Jan 21;12(2):101. doi:10.3390/metabo12020101

60. Doni D, Cavion F, Bortolus M, Baschiera E, Muccioli S, Tombesi G, et al. Human frataxin, the Friedreich ataxia deficient protein, interacts with mitochondrial respiratory chain. Cell Death Dis. 2023 Dec 8;14(12):805. doi:10.1038/s41419-023-06320-y

61. Klemmensen MM, Borrowman SH, Pearce C, Pyles B, Chandra B. Mitochondrial dysfunction in neurodegenerative disorders. Neurotherapeutics. 2024 Jan;21(1):e00292. doi:10.1016/j.neurot.2023.10.002

62. Loesch DZ, Annesley SJ, Trost N, Bui MQ, Lay ST, Storey E, et al. Novel Blood Biomarkers Are Associated with White Matter Lesions in Fragile X- Associated Tremor/Ataxia Syndrome. Neurodegener Dis. 2017;17(1):22–30. doi:10.1159/000446803

63. Nobile V, Palumbo F, Lanni S, Ghisio V, Vitali A, Castagnola M, et al. Altered mitochondrial function in cells carrying a premutation or unmethylated full mutation of the FMR1 gene. Hum Genet. 2020 Feb;139(2):227–45. doi:10.1007/s00439-019-02104-7

Supplementary Files

This is a list of supplementary files associated with this preprint. Click to download.

- SupplementaryTable2.xlsx
- Supplementalfigure2.tif
- Supplementaryfigure1.tif
- SupplementaryTable1.xlsx
- 20251205gelApolyGPgreen70KDA.NiCgfpMOSCA36GPSCA36GPMOnop56lowMOnop56MOnop56low.tif
- 20251205gelAbactinrb42KDAgreen.NiCgfpMOSCA36GPSCA36GPMOnop56lowMOnop56MOnop56low.tif